HOMOTOPY ANALYSIS OF MAGNETOHYDRODYNAMIC CONVECTION FLOW IN MANUFACTURE OF A VISCOELASTIC FABRIC FOR SPACE APPLICATIONS

O.Anwar Bég [1], U. S. Mahabaleshwar[2], M. M. Rashidi [3], N. Rahimzadeh [3], J-L Curiel Sosa [4]
Ioannis Sarris[5] and N. Laraqi[6]

[1] *Gort Engovation Research (Propulsion and Biomechanics), 15 Southmere Avenue, Bradford, West Yorkshire BD7 3NU, UK.*
[2] *Deartment of Mathematics, Government First Grade College for Women, Hassan -573 201, INDIA.*

[3] *Mechanical Engineering Department, Bu-Ali Sina University, Hamedan, IRAN.*

[4] *Mechanical Engineering, University of Sheffield, Portobello Centre, B66, Sheffield,S13JD,UK*
[5] *Department of Energy Technology, Technological & Educational Institute of Athens, 17 Ag. Spyridona Str., 12210 Athens, GREECE,*
[6] *Laboratoire TIE, Department GTE, Universite Paris 10, EA 4415, 50 Rue de Sevres, F92410 Ville d'Avray, FRANCE*

Received 18 April 2012; accepted 23 March 2013

ABSTRACT

Aerospace electro-conductive polymer materials are a new family of “smart” materials being deployed in many complex applications. The precision manufacturing of such processes to manipulate properties and enhance performance can exploit magnetohydrodynamic (MHD) control and simultaneous heat transfer (thermal processing). Motivated by these applications, we develop a model for laminar free convective flow of an incompressible and electrically-conducting viscoelastic fluid (Walters’ liquid B) over a continuously moving stretching surface embedded in a porous medium in the presence of strong radiative heat flux, as a simulation of magnetic smart fabric sheet processing. A heat generation/absorption term is included in the model. Darcy’s law is used to simulate porous media bulk drag effects. The stretching is assumed to be a linear function of the coordinate along the direction of stretching. Using similarity transformations, the governing partial differential equations are converted to nonlinear ordinary differential equations. The energy equation is further rendered into confluent hypergeometric form and then solved analytically for the prescribed surface temperature (PST) case and also for the Prescribed Boundary Surface Heat Flux (PHF) case, using Kummer’s function, subject to physically realistic boundary conditions. The momentum and energy equations are also solved using the semi-numerical homotopy analysis method (HAM), which contains the auxiliary parameter $\hbar$, permitting relatively easy adjustment and control of the convergence region of the series solution. This method provides an efficient approximate analytical solution with high accuracy, minimal calculation, and avoidance of physically unrealistic assumptions. HAM solutions are benchmarked with robust numerical shooting quadrature and found to correlate well. The influence of magnetic field on velocity

and temperature profiles is studied via the Chandrasekhar number (Q). Furthermore detailed simulations are conducted for the influence of viscoelastic parameter (k_1), Eckert number (E), radiation-conduction parameter (N_R), Grashof number (Gr) and heat source/sink parameter (α) on the flow variables. The study finds applications in electro-conductive polymeric materials processing for aerospace fabric covers and other applications with demanding safety and protection requirements in smart materials synthesis.

Keywords: Magnetohydrodynamics, Viscoelasticity; Homotopy, Radiation; Semi-numerical, Electro-conductive polymer materials processing; Heat Transfer; Chandrasekhar number

1 INTRODUCTION

Recent progress in "smart fabrics" has stimulated renewed interest in magnetohydrodynamic (MHD) materials processing. The augmentation of high strength fabrics with non-Newtonian fluids is being seriously explored as a mechanism for enhancing ballistic performance of fragment barrier materials widely used in spacecraft orbital debris shielding, and other applications (Son and Hahrenthold 2012). Magnetorheological (MR) fluids are especially useful in such areas since they demonstrate excellent controllability. The simulation of synthesis of such materials and also electro-conductive smart/interactive textiles (SMITs) poses a rich area for numerical simulation (Das et al. 2010). The tremendous potential of conductive polymers for future applications in astronaut suits, biochemical hazard protection, physiological status monitoring and other systems in space science, requires ever more sophisticated modeling techniques for accurately predicting performance and characteristics of such materials.

The flow and heat transfer analysis in the boundary layer on a continuously moving or stretching surface is a key mechanism used MHD materials processing. The pioneering work on the continuously stretching sheet was first initiated by Sakiadis (1961). The so-called "Sakiadis flow" has subsequently been extended to consider more complex thermophysical and geometrical effects by many researchers including Crane (1970), Gupta and Gupta (1977), McLeod and Rajagopal (1987), Banks (1983), Dutta et al. (1985), Chen and Char (1988), Ali (1995), and Liao (2005). In these studies, a linear velocity of the surface is implicit in the model. Furthermore a number of articles have addressed heat transfer from a continuously moving flat plate, for example Tsou et al. (1967), Erickson et al. (1966), Griffin and Throne (1967) and Horvay (1961) and a circular cylinder, see for example Anderson (1958), Arridge and Prior (1964),Griffith (1964), Glicksman (1968), Alderson et al. (1968), Vasudevan and Middleman (1970), Bourne and Elliston (1970), Bourne and Dixon (1971), Horvay and Dacosta (1964). These papers have considered various surface conditions including constant surface temperature or constant heat flux and that the moving solid and the fluid are conjugated through surface thermal conditions. According to the general characteristics of conjugate heat-transfer problems (Chida and Katto 1976), in heat transfer from a continuously moving surface, the combination of physical properties of the moving solid and the surrounding fluid exerts a key role. The flow domain is an unsteady one from a viewpoint of the coordinate system fixed to the moving solid. However in previous investigations under conjugated conditions, the theoretical analysis has neglected heat conduction in the solid (Bourne and Dixon, 1971) and experiments have been carried out only for the drawing of glass fibres in air (Anderson, 1958, Arridge and Prior, 1964 and Alderson et al., 1968). Mathematical models of stretching sheet flows of for example electro-conductive polymers,

must therefore feature a robust viscoleastic formulation. A rich variety of such models exist including Reiner Rivlin differential models of second order (Bég et al. 2004) and 3rd order (Bég et al, 2008a), Maxwell upper convected models (Bég and Makinde, 2011) and Eringen micropolar models (Bég et al, 2011a,b,c). An important class of non-Newtonian model is the Walters-B liquid model which is a robust formulation for certain polymeric materials exhibiting short-term viscoelastic effects. Abel et al. (2007) investigated the non-Newtonian viscoelastic boundary layer flow of Walters' liquid B past a stretching sheet, considering non-uniform heat source and frictional heating, Abel and Nandeppanavar (2007) studied the effects of thermal radiation and non-uniform heat source on MHD flow of viscoelastic boundary layer flow. Abel and Nandeppanavar (2008) further reported on the influence of variable thermal conductivity and non-uniform heat source on viscoelastic boundary layer flow. Further studies using the Walters' liquid B include Abel and Nandeppanavar (2009) for non-uniform heat source effects on MHD flow, Abel et al. (2008) for the effects of viscous and Ohmic dissipation in MHD flow of viscoelastic boundary layer flow and Abel and Nandeppanavar (2008). Very recently Bég et al. (2011d) have used the Walters'-B viscoelastic model to study the transient free convection of a conducting polymer in a Darcy-Forchheimer porous medium using network simulation.

Many powerful methods proposed to solve these similarity solution equations. With numerical method, stability and convergence are imperative to avoid divergence or inappropriate results. In the analytical perturbation method, a small parameter is required, and this imposes severe limitations on such methods. A semi-exact method which circumvents the need for small or large perturbation parameters is HAM, proposed by Liao (2003). This method has already been applied successfully to solve many complex problems in hydromagnetics and porous media transport phenomena as studied by Wang et al. (2003a), Wang et al. (2003b). It has also been implemented in numerous industrial thermofluid flow problems and some examples include the papers by Akyildiz et al. (2009), Liao (1999), Domairry et al. (2009), Domairry and Nadim (2008), Domairry and Fazeli (2009). HAM allows the adjustment and control of the convergence region and this is the most attractive feature of this technique in comparison with other techniques (Liao, 2009). It should be emphasized that the so-called homotopy perturbation method (HPM) as studied by Alizadeh-Pahlavan and Borjian-Boroujeni (2008), Sajid and Hayat (2008), Wanga et al. (2008), and Chowdhury et al. (2009) is only a special case of HAM. More details of this are given in Dinarvand and Rashidi (2010), Rashidi et al. (2011), Rashidi and Mohimanian pour (2010), Rashidi et al. (2009) and He (2006).

In the present work, we consider the multi-physical laminar free convective flow of an incompressible and electrically conducting viscoelastic fluid (Walters' liquid) over a continuously moving stretching surface embedded in a porous medium. Rosseland's model is employed to simulate radiative heat transfer. Darcy's law is used to model the porous media fiber impedance. Viscoelasticity is simulated using the robust Walters' B rheological model which has shown exceptional accuracy in predicting the flow characteristics of certain polymers. This problem is important in the simulation of synthesis processes of novel "intelligent" materials for astronautical applications. The transformed, dimensionless equations are solved analytically with Kummer functions and also with the semi-numerical HAM approach. Additionally the HAM solutions are further validated with numerical quadrature. Moreover the powerful ability of HAM as an alternative tool to purely numerical methods, in multi-physical fluid dynamics is demonstrated.

2 MATHEMATICAL FORMULATION AND ANALYSIS

We consider a steady, two-dimensional boundary layer flow of an incompressible and electrically conducting isothermal viscoelastic Walters' liquid B over a linear stretching sheet within a porous medium (see Fig.1A). Further details are provided in the 3-D schematic in Fig. 1B. Two equal and opposite forces are applied along the x-axis so that the sheet is stretched keeping the origin fixed. A uniform, static, transverse magnetic field B_0 is applied along the y-axis on the weak electrically conducting liquid occupying the half space y>0. The magnetic Reynolds number is small and hence the induced magnetic field is negligible as compared to the applied magnetic field. Ionslip and Hall current effects are therefore also neglected (Bég et al. 2011d).

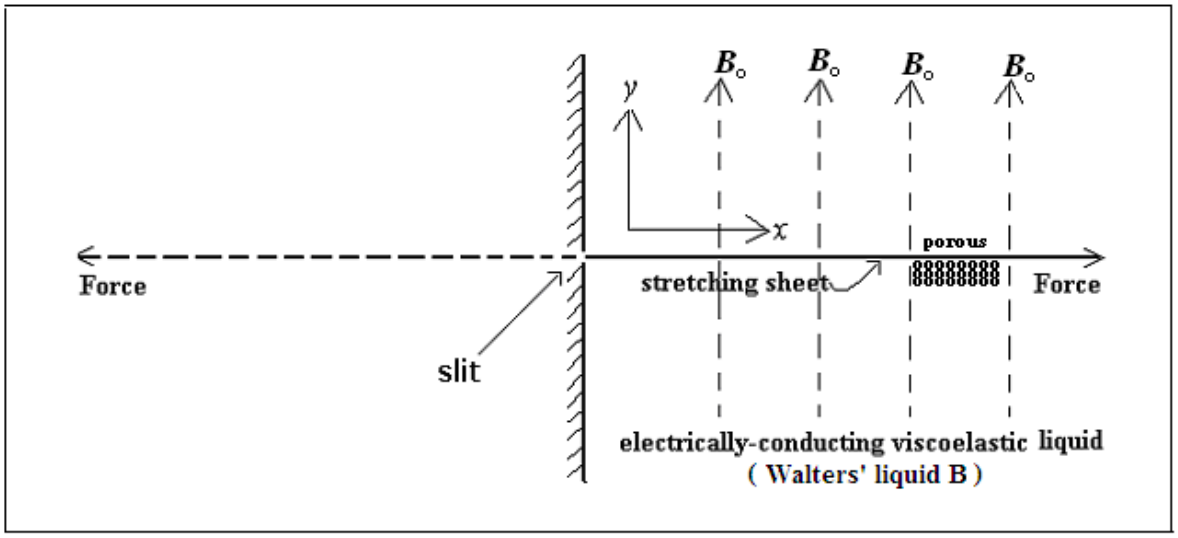

Figure 1A: Schematic diagram of the stretching sheet problem.

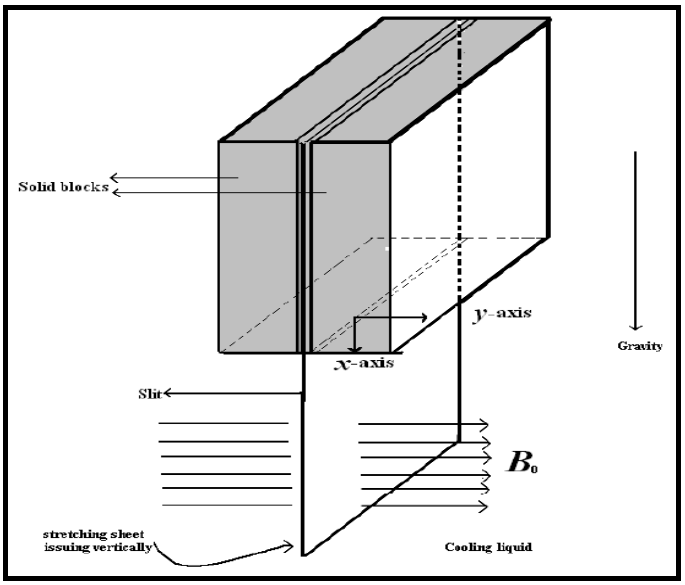

Figure 1B: Physical configuration.

A unidirectional radiative flux acts transverse to the sheet. The Walters' liquid B is a model for short or rapidly fading memory liquids and is thus an approximation based on first order elasticity. The liquid is at rest and the motion is effected by pulling the sheet on both ends with equal forces parallel to the sheet and with a speed u, which varies linearly with the distance from the slit as, $u = cx$. The resulting motion of the otherwise quiescent liquid is thus generated solely by the moving sheet. The steady, two-dimensional conservation of mass and the momentum boundary layer equations for the linearly stretching sheet problem involving Walters' liquid B are:

Continuity Equation

$$\frac{\partial u}{\partial x} + \frac{\partial v}{\partial y} = 0, \tag{1}$$

Conservation of Momentum

$$u\frac{\partial u}{\partial x} + v\frac{\partial u}{\partial y} = \gamma\frac{\partial^2 u}{\partial y^2} - k_o\left\{u\frac{\partial^3 u}{\partial x\,\partial y^2} + v\frac{\partial^3 u}{\partial y^3} + \frac{\partial u}{\partial x}\frac{\partial^2 u}{\partial y^2} - \frac{\partial u}{\partial y}\frac{\partial^2 u}{\partial x\,\partial y}\right\} - \left(\frac{\sigma B_o^2}{\rho} - \frac{\nu}{k'}\right)u + g\beta\left(T - T_\infty\right). \tag{2}$$

Here x and y are respectively the directions along and perpendicular to the surface, u, v are the velocity components along the x and y directions respectively and the other symbols are documented in the nomenclature. The last term in equation (2) corresponds to thermal buoyancy. The second component of the penultimate term in (2) is the Darcian linear drag force, which is accurate for slow, viscous-dominated flows (Bég et al. 2010, 2011e). The first component is the Lorentzian magnetohydrodynamic drag force. In deriving these equations, it is assumed, in addition to the usual boundary layer approximations that the contribution due to the normal stress is of the same order of magnitude as the shear stress.

The boundary conditions applicable to the flow problem are:

$$\begin{array}{llll} u = cx, & v = 0, & T = T_w\left(x\right) & \text{at} \quad y = 0 \\ u \to 0, & u_y \to 0, T \to T_\infty & & \text{as} \quad y \to \infty, \end{array} \tag{3}$$

Equations (1) and (2) admit self-similar solutions of the form:

$$u = c\,x\,f_\eta(\eta), \qquad v = -\sqrt{c\,\gamma}\,f\,(\eta), \qquad \theta(\eta) = \frac{T - T_\infty}{T_w - T_\infty}, \qquad \eta = \sqrt{\frac{c}{\gamma}}\,y\,, \tag{4}$$

where subscript η denotes the derivative with respect to η. Clearly u and v satisfy the equation (1) identically. Substituting these new variables in equation (2), we have

$$f_\eta^{\,2} - f\,f_{\eta\eta} = f_{\eta\eta\eta} - k_1\left\{2f_\eta\,f_{\eta\eta\eta} - f\,f_{\eta\eta\eta\eta} - f_{\eta\eta}^{\,2}\right\} - \left(Q + D_a^{-1}\right)f_\eta + Gr\,\theta. \tag{5}$$

where $k_1 = \frac{k_0 c}{\mu}$ is viscoelastic parameter, $D_a^{-1} = \frac{c\,k'}{\gamma}$ is inverse Darcy number, $Q = B_0^2 \frac{\sigma}{c\rho}$ is Chandrasekhar hydromagnetic number, $Gr = \frac{g\,\beta A}{c^2 l}$ is Grashof number. The transformed boundary conditions (3) take the form

$$\begin{aligned} &f_\eta(\eta)=1, \quad f(\eta)=0, \quad \theta(\eta)=1 \quad \text{at} \quad \eta=0 \\ &f_\eta(\eta)\to 0, \quad f_{\eta\eta}(\eta)\to 0, \quad \theta(\eta)\to 0 \quad \text{as} \quad \eta\to\infty. \end{aligned} \tag{6}$$

If $Gr = D_a^{-1} = 0$, the governing boundary layer heat transport equation with viscous dissipation, temperature-dependent internal heat generation and radiation flux is:

$$u\frac{\partial T}{\partial x} + v\frac{\partial T}{\partial y} = \alpha^* \frac{\partial^2 T}{\partial y^2} + \frac{\mu}{\rho C_p}\left(\frac{\partial u}{\partial y}\right)^2 + \frac{Q^*}{\rho C_p}(T - T_\infty) - \frac{1}{\rho C_p}\frac{\partial q_r}{\partial y}. \tag{7}$$

By using Rosseland's diffusion approximation for radiation, the radiative heat flux, q_r is given by:

$$q_r = -\frac{4\sigma^*}{3k^*}\frac{\partial\left(T^4\right)}{\partial y}. \tag{8}$$

where σ* is the Stefan-Boltzmann constant and k* is the spectral mean absorption coefficient of the medium. This model is valid for optically-thick media in which thermal radiation propagates only a limited distance prior to experiencing scattering or absorption. The local thermal radiation intensity is due to radiation emanating from proximate locations in the vicinity of which emission and scattering are comparable to the location of interest. For zones where conditions are appreciably different thermal radiation has been shown to be greatly attenuated before arriving at the location under consideration as discussed by Viskanta (1963). The energy transfer depends on conditions only in the area adjacent to the plate regime i.e. the boundary layer regime. Rosseland's model yields accurate results for intensive absorption i.e. optically-thick flows which are optically far from the bounding surface. Implicit in this approximation is also the existence of wavelength regions where the optical thickness may exceed a value of five. As such the Rosseland model, while limited compared with other flux models, can simulate to a reasonable degree of accuracy thermal radiation in problems ranging from thermal radiation transport via gases at low density to thermal radiation simulations associated with nuclear blast waves (Chandrasekhar, 1960; Bég et al. 2009a, 2009b, Takhar et al. 2003). Rosseland's model therefore simulates accurately materials processing flows and is a valid approach for "intensive absorption" which is encountered in such systems. It is assumed that $\frac{\partial q_r}{\partial y} >> \frac{\partial q_r}{\partial x}$. For boundary layer flows with convection and radiation the x-direction radiative flux, $\frac{\partial q_r}{\partial x} << \rho C_p u \frac{\partial T}{\partial x}$. This effectively implies that the dominant radiative flux is the term, $\frac{\partial q_r}{\partial y}$ and this is why the $\frac{\partial q_r}{\partial x}$ term is neglected in the

analysis (it has negligible contribution). We now expand T^4 in a Taylor series about T_∞ as follows:

$$T^4 = T_\infty^4 + 4T_\infty^3 (T - T_\infty) + 6T_\infty^2 (T - T_\infty)^2 + \cdots . \tag{9}$$

Neglecting higher-order terms in the above equation beyond the first degree in $(T - T_\infty)$, we get:

$$T^4 \cong -3T_\infty^4 + 4T_\infty^3 T. \tag{10}$$

By employing Equations (8) and (10), Equation (7) becomes:

$$u\frac{\partial T}{\partial x} + v\frac{\partial T}{\partial y} = \left(\alpha^* + \frac{16\sigma^* T_\infty^3}{3\rho C_p k^*}\right)\frac{\partial^2 T}{\partial y^2} + \frac{\mu}{\rho C_p}\left(\frac{\partial u}{\partial y}\right)^2 + \frac{Q^*}{\rho C_p}(T - T_\infty). \tag{11}$$

From the above equation it is apparent that the effect of radiation is to augment the thermal diffusivity. The thermal boundary conditions for solving Equation (11) depend on the type of heating process under consideration. We consider two different heating processes, namely:

(a) Prescribed Surface Temperature (PST)

And

(b) Prescribed wall Heat Flux (PHF).

(a) Prescribed Surface Temperature (PST)

The prescribed power law surface temperature is considered to be a power of x in the form

$$\left.\begin{array}{lll} T = T_w = T_\infty + A\left(\dfrac{x}{l}\right)^s & \text{at} & y = 0 \\ T \to T_\infty & \text{as} & y \to \infty \end{array}\right\}, \tag{12}$$

where A is a constant and l is the characteristic length.

We now define a non-dimensional temperature $\theta(\eta)$ as:

$$\theta(\eta) = \frac{T - T_\infty}{T_w - T_\infty}, \tag{13}$$

where

$$T - T_\infty = A\left(\frac{x}{l}\right)^s \theta(\eta) \text{ and } T_w - T_\infty = A\left(\frac{x}{l}\right)^s .$$

Substitution of Equation (13) in the energy equation (11) leads to the following equation:

$$(1+N_R)\ \theta'' + \frac{\Pr}{\beta}\left(1-Exp[-\beta\eta]\right)\theta' - \Pr\left(s\ Exp[-\beta\eta]-\alpha\right)\theta$$
$$= -\Pr E\ (x\ l)^{s-2}\ \beta^2\, Exp[-2\beta\eta], \tag{14}$$

where prime denotes differentiation with respect to η.

In due course, we readily obtain an x −independent similarity equation from the above when $s=2$ and this yields:

$$(1+N_R)\ \theta'' + \frac{\Pr}{\beta}\left(1-Exp[-\beta\eta]\right)\theta' - \Pr\left(2\ Exp[-\beta\eta]-\alpha\right)\theta = -\Pr E\ \ \beta^2\, Exp[-2\beta\eta]. \tag{15}$$

The boundary condition in terms of θ can be obtained from Equations (12) and (13) as

$$\left.\begin{array}{lll} \theta = 1 & \text{at} & \eta = 0 \\ \theta \to 0 & \text{as} & \eta \to \infty \end{array}\right\}. \tag{16}$$

Equation (15) is linear in θ and we now transform the same into a confluent hypergeometric equation by using the following transformation:

$$\xi = -R\ \ Exp[-\beta\,\eta]. \tag{17}$$

Substituting Equation (17) into Equation (15), we get

$$(1+N_R)\ \ \xi\ddot{\theta} + \left[\ 4(1+N_R) - R - \xi\ \right]\ \dot{\theta} + \left(2+\frac{R\alpha}{\xi}\right)\theta = -\Pr E\ \frac{\xi}{R^2}, \tag{18}$$

where the overdot denotes differentiation with respect to ξ.

The boundary conditions in Equation (16), in terms of ξ translate to:

$$\theta\left(\xi = -R\right) = 1 \quad \text{and} \quad \theta(0) = 0. \tag{19}$$

The solution of Equation (18) satisfying the conditions (19) in terms of Kummer's function are:

$$\theta(\xi)=\frac{\left\{1+\Pr E\left[4(1+N_R)-2R+R\,\alpha\right]^{-1}\right\}\left(\frac{-\xi}{R}\right)^{\left(\frac{\lambda_1+d_1}{2}\right)}F\left[\frac{\lambda_1+d_1-4}{2},\ d_1+1,\ \xi\right]}{F\left[\frac{\lambda_1+d_1-4}{2},\ d_1+1,\ -R\right]} \tag{20}$$

$$-\Pr E\left[4(1+N_R)-2R+R\,\alpha\right]^{-1}\left(\frac{\xi}{R}\right)^2.$$

The solution of Equation (20) can be written in terms of η as

$$\theta(\eta)=\frac{\left\{1+\Pr E\left[4(1+N_R)-2R+R\,\alpha\right]^{-1}\right\}e^{-\beta\eta\left(\frac{\lambda_1+d_1}{2}\right)}F\left[\frac{\lambda_1+d_1-4}{2},\ d_1+1,-R*e^{-\beta\eta}\right]}{F\left[\frac{\lambda_1+d_1-4}{2},\ d_1+1,\ -R\right]} \tag{21}$$

$$-\Pr E\left[4(1+N_R)-2R+R\,\alpha\right]^{-1}*e^{-2\beta\eta}.$$

The non-dimensional wall temperature gradient derived from Equation (13) is

$$\dot{\theta}(0)=\frac{\left\{1+\Pr E\left[4(1+N_R)-R+R\ \alpha\right]^{-1}\right\}}{F\left[\frac{\lambda_1+d_1-4}{2},d_1+1,-R\right]}\times$$

$$\left\{\begin{array}{l}-\beta\left(\frac{\lambda_1+d_1}{2}\right)F\left[\frac{\lambda_1+d_1-4}{2},d_1+1,-R\right]+\frac{R\,\beta}{2}\left(\frac{\lambda_1+d_1-4}{d_1+1}\right)\\ F\left[\frac{\lambda_1+d_1-2}{2},d_1+2,-R\right]\end{array}\right\} \tag{22}$$

$$+2\beta\Pr E\left[4(1+N_R)-2R+R\ \alpha\right]^{-1},$$

and the local heat flux can be expressed as

$$q_w=-k\left(\frac{\partial T}{\partial x}\right)_{y=0}=-k\,A\sqrt{\frac{c}{\nu}}\left(\frac{x}{l}\right)^2\dot{\theta}(0). \tag{23}$$

The expressions in Equation (21) and Equation (22) are numerically evaluated for several values of the parameters E, k_1, N_R, Pr, Q and α and the results are discussed in the last section. We now move on to discuss the case of a temperature boundary condition involving a prescribed wall heat flux.

(b) Prescribed wall Heat Flux (PHF)

The power law heat flux on the wall surface is considered to be a power of x in the form:

$$\left.\begin{array}{lll} -k\dfrac{\partial T}{\partial y} = q_w = D\left(\dfrac{x}{l}\right)^s & \text{at} & y=0 \\ T \to T_\infty & \text{as} & y \to \infty \end{array}\right\}, \tag{24}$$

where D is a constant and l is the characteristic length. We now define a non-dimensional temperature $g(\eta)$ as:

$$g(\eta) = \frac{T - T_\infty}{T_w - T_\infty}, \tag{25}$$

Where

$$T - T_\infty = \frac{D}{k}\left(\frac{x}{l}\right)^s \sqrt{\frac{\nu}{c}}\; g(\eta),$$

and (26)

$$T_w - T_\infty = \frac{D}{k}\left(\frac{x}{l}\right)^s \sqrt{\frac{\nu}{c}}.$$

In spite of the fact that $g(\eta)$ in Equation (25) is the same as $\theta(\eta)$ defined in Equation (15) for PST case, we prefer to use a different notation for the PHF case. Substitution of Equation (25) in the energy equation (11) leads to the following equation:

$$(1+N_R)\,g'' + \frac{\Pr}{\beta}\left(1 - Exp[-\beta\eta]\right)\,g' - \Pr\left(s\;Exp[-\beta\eta] - \alpha\right)\theta = -\Pr E_s\,(x\,l)^{s-2}\;\beta^2\,Exp[-2\beta\eta]. \tag{27}$$

Obviously, we get an x −independent similarity equation from the above when $s = 2$ and this yields:

$$(1+N_R)\;g'' + \frac{\Pr}{\beta}\left(1 - Exp[-\beta\eta]\right)\,g' - \Pr\left(2\;Exp[-\beta\eta] - \alpha\right)g = -\Pr E_s\;\beta^2\,Exp[-2\beta\eta]. \tag{28}$$

The boundary conditions in terms of g can be obtained from Equations (24) and (25) as

$$g'(0) = -1 \quad \text{and} \quad g(\infty) = 0, \tag{29}$$

where prime denotes differentiation with respect to η and all other parameters are as defined in the PST case, but wherever is involved in the equations of PST case it is to be replaced by D of PHF. Substituting Equation (17) into Equations (28) and (29), we get:

$$(1+N_R)\,\xi\,\ddot{g} + \left[4(1+N_R) - R - \xi\right]\dot{g} + \left(2 + \frac{R\alpha}{\xi}\right)g = -\frac{\Pr E_s}{R^2}\,\xi, \tag{30}$$

$$\dot{g}(-R) = -\frac{1}{R\beta} \quad \text{and} \quad \mathrm{g}(0) = 0, \tag{31}$$

where the overdot denotes differentiation with respect to ξ. Equation (30) is a confluent hypergeometric equation and the solution for g satisfying Equation (31) is obtained in terms of Kummer's function as:

$$\begin{aligned} g(\xi) = & \left[\frac{1}{\beta} + \frac{2\Pr E_s}{\left(4(1+N_R) - 2R + R\alpha\right)}\right] \\ & * \left\{\frac{\lambda_1 + d_1}{2} F\left[\frac{\lambda_1 + d_1 - 4}{2}, d_1 + 1, -R\right] - R\,\dot{F}\left[\frac{\lambda_1 + d_1 - 4}{2}, d_1 + 1, -R\right]\right\}^{-1} \\ & * \left(\frac{-\xi}{\mathrm{R}}\right)^{\left(\frac{\lambda_1 + d_1}{2}\right)} F\left[\frac{\lambda_1 + d_1 - 4}{2},\ d_1 + 1,\ -\xi\right] - \frac{\Pr E_s}{\left(4(1+N_R) - 2R + R\alpha\right)}\left(\frac{\xi}{\mathrm{R}}\right)^2, \end{aligned} \tag{32}$$

where the function $\dot{F}$ satisfies the relationship $\dot{F}[a, b, z] = \frac{a}{b} F[a+1, b+1, z]$ and the other terms are as defined earlier. In terms of η, the expression for g is

$$\begin{aligned} g(\eta) = & \left[\frac{1}{\beta} + \frac{2\Pr E_s}{\left[4(1+N_R) - 2R + R\alpha\right]}\right] \\ & * \left\{\frac{\lambda_1 + d_1}{2} F\left[\frac{\lambda_1 + d_1 - 4}{2}, d_1 + 1, -R\right] - R\,F'\left[\frac{\lambda_1 + d_1 - 4}{2}, d_1 + 1, -R\right]\right\}^{-1} \\ & * \mathrm{Exp}\left[-\beta\left(\frac{\lambda_1 + d_1}{2}\right)\eta\right] F\left[\frac{\lambda_1 + d_1 - 4}{2},\ d_1 + 1,\ -R\,Exp(-\beta\eta)\right] - \frac{\Pr E_s \quad Exp(-2\beta\eta)}{\left[4(1+N_R) - 2R + R\alpha\right]}. \end{aligned} \tag{33}$$

The wall temperature T_w is obtained from Equation (26) as

$$T_w - T_\infty = \frac{D}{k}\left(\frac{x}{l}\right)^2 \sqrt{\frac{\nu}{c}}\, g(0). \tag{34}$$

3 FUNDAMENTAL CONSTRUCTS OF HAM

HAM has emerged as a tremendously versatile semi-numerical method for nonlinear fluid dynamics. Introduced by Liao (2003), it has been deployed in resolving an increasingly broad spectrum of complex multi-physical flow problems. HAM has exceptional stability and convergence features. It has been used in viscoelastic gastric flowst (Tripathi et al. 2012), transient helicopter swirl flows (Mehmood et al. 2010), nanofluid dynamics (Bég et al. 2012; and magnetohydrodynamic entropy generation flows (Bég et al. 2013). Let us consider the following differential equation:

$$\mathcal{N}[u(\tau)] = 0, \tag{35}$$

Where N is a nonlinear operator, τ denotes independent variable, $u(\tau)$ is an unknown function, respectively. For simplicity, we ignore all boundary or initial conditions, which can be treated in the similar way. By means of generalizing the traditional homotopy method, Liao (2003) constructs the so-called zero-order deformation equation:

$$(1-p)\mathcal{L}\left[\varphi(\tau;p)-u_0(\tau)\right]=p\,\hbar H(\tau)\mathcal{N}\left[\varphi(\tau;p)\right], \tag{36}$$

where $p\in[0,1]$ is the embedding parameter, $\hbar\neq 0$ is a non-zero auxiliary parameter, $H(\tau)\neq 0$ is an auxiliary function, $\mathcal{L}$ is an auxiliary linear operator, $u_0(\tau)$ is an initial guess of $u(\tau)$, $\varphi(\tau;p)$ is an unknown function, respectively. It is important, that one has great freedom to choose auxiliary parameters with HAM. When $p=0$ and $p=1$, it holds $\varphi(\tau;0)=u_0(\tau)$, $\varphi(\tau;1)=u(\tau)$, respectively. Thus as p increases from 0 to 1, the solution $\varphi(\tau;p)$ varies from the initial guess $u_0(\tau)$ to the solution $u(\tau)$. Expanding $\varphi(\tau;p)$ in Taylor series with respect to p, we have:

$$\varphi(\tau;p)=u_0(\tau)+\sum_{m=1}^{+\infty}u_m(\tau)p^m, \tag{37}$$

where

$$u_m(\tau)=\frac{1}{m!}\frac{\partial^m\varphi(\tau;p)}{\partial p^m}\bigg|_{p=0}. \tag{38}$$

If the auxiliary linear operator, the initial guess, the auxiliary parameter $\hbar$, and the auxiliary function are so properly chosen, the series eqn. (37) converges at $p=1$, then we have

$$u(\tau)=u_0(\tau)+\sum_{m=1}^{+\infty}u_m(\tau), \tag{39}$$

which must be one of solutions of original nonlinear equation, as proved by Liao [36]. As $\hbar=-1$ and $H(\tau)=1$ equation (36) becomes:

$$(1-p)\mathcal{L}\left[\varphi(\tau;p)-u_0(\tau)\right]+p\mathcal{N}\left[\varphi(\tau;p)\right]=0, \tag{40}$$

which is implemented mostly in the homotopy perturbation method (HPM), where the solution obtained directly, without using Taylor series as elucidated by He (2000) and Öziş and Yıldırım (2007). According to the definition (38), the governing equation can be deduced from the zero-order deformation equation (35). Defining the vector $\vec{u}_n=\left\{u_0(\tau),u_1(\tau),\ldots,u_n(\tau)\right\}$ and differentiating equation (35) m times with respect to the embedding parameter p and then setting $p=0$ and finally dividing them by $m!$, we have the so-called mth-order deformation equation

$$\mathcal{L}\left[u_m(\tau)-\chi_m u_{m-1}(\tau)\right]=\hbar H(\tau)R_m(\vec{u}_{m-1}), \tag{41}$$

Where

$$R_m(\vec{u}_{m-1}) = \frac{1}{(m-1)!}\frac{\partial^{m-1}\mathcal{N}\left[\varphi(\tau;p)\right]}{\partial p^{m-1}}\bigg|_{p=0}, \tag{42}$$

And

$$\chi_m = \begin{cases} 0, & m \le 1, \\ 1, & m > 1. \end{cases}$$

It should be emphasized that $u_m(\tau)$ for $m \ge 1$ is governed by the linear equation (41) with the linear boundary conditions that come from original problem, which can be easily solved by symbolic computation software such as Maple and Mathematica.

4 HAM SOLUTION: MAGNETO-VISCOELASTIC CONVECTIVE-RADIATIVE FLOW

In this section we apply the HAM to obtain approximate analytical solutions for the problem outlined in section 2. i.e. equations (5), (15) and (28). We start with initial approximation $f_0(\eta) = \eta Exp[-\eta],\ \theta_0(\eta) = Exp[-\eta],\ g_0(\eta) = Exp[-\eta]$ and a linear operator defined thus:

$$\mathcal{L}\left[f(\eta;p)\right] = \frac{\partial^3 f(\eta;p)}{\partial \eta^3} - \frac{\partial f(\eta;p)}{\partial \eta}, \tag{43}$$

$$\mathcal{L}\left[\theta(\eta;p)\right] = \frac{\partial^2 \theta(\eta;p)}{\partial \eta^2} - \theta(\eta;p), \tag{44}$$

$$\mathcal{L}\left[g(\eta;p)\right] = \frac{\partial^2 g(\eta;p)}{\partial \eta^2} - g(\eta;p), \tag{45}$$

Furthermore, equations (5), (15) and (28) suggests we define the nonlinear operator:

$$\begin{aligned}\mathcal{N}\left[f(\eta;p)\right] = k_1\Bigg(&2\frac{\partial f(\eta;p)}{\partial \eta}\frac{\partial^3 f(\eta;p)}{\partial \eta^3} - f(\eta;p)\frac{\partial^4 f(\eta;p)}{\partial \eta^4} - \frac{\partial^2 f(\eta;p)}{\partial \eta^2}\frac{\partial^2 f(\eta;p)}{\partial \eta^2}\Bigg) \\ &+ \frac{\partial^2 f(\eta;p)}{\partial \eta^2}\frac{\partial^2 f(\eta;p)}{\partial \eta^2} - f(\eta;p)\frac{\partial^2 f(\eta;p)}{\partial \eta^2} - \frac{\partial^3 f(\eta;p)}{\partial \eta^3} \\ &- (Q + Da^{-1})\frac{\partial f(\eta;p)}{\partial \eta} + Gr\ \theta(\eta;p),\end{aligned} \tag{46}$$

$$\begin{aligned}\mathcal{N}\left[\theta(\eta;p)\right] = &(1+N_R)\frac{\partial^2 \theta(\eta;p)}{\partial \eta^2} + \frac{Pr}{\beta}(1 - Exp[-\beta\eta])\frac{\partial \theta(\eta;p)}{\partial \eta} \\ &+ Pr(2Exp[-\beta\eta] - \alpha)\theta(\eta;p) + Pr\ E\ \beta^2\ Exp[-2\beta\eta],\end{aligned} \tag{47}$$

$$\mathcal{N}\left[g(\eta;p)\right]=(1+N_R)\frac{\partial^2 g(\eta;p)}{\partial\eta^2}+\frac{Pr}{\beta}(1-Exp[-\beta\eta])\frac{\partial g(\eta;p)}{\partial\eta}$$
$$+Pr(2Exp[-\beta\eta]-\alpha)g(\eta;p)+Pr\ E\ \beta^2\ Exp[-2\beta\eta], \tag{48}$$

using the above definition, with assumption $H_f(\tau)=Exp[-\eta]$, $H_\theta(\tau)=Exp[-\eta]$, $H_g(\tau)=Exp[-\eta]$, we construct the zero-order deformation equation

$$(1-p)\mathcal{L}\left[\varphi(x;p)-u_0(x)\right]=Exp[-\eta]p\,\hbar\,\mathcal{N}\left[\varphi(x;p)\right]. \tag{49}$$

Obviously, when $p=0$ and $p=1$,

$$\varphi(x;0)=u_0(x),\qquad \varphi(x;1)=u(x). \tag{50}$$

Differentiating the *zero*th-order deformation equation (47) m times with respect to p, and finally dividing by $m!$, we have the mth-order deformation equation

$$\mathcal{L}\left[f_m(x)-\chi_m f_{m-1}(x)\right]=Exp[-\eta]\hbar R_m(\vec{f}_{m-1}), \tag{51}$$

$$\mathcal{L}\left[\theta_m(x)-\chi_m \theta_{m-1}(x)\right]=Exp[-\eta]\hbar R_m(\vec{\theta}_{m-1}), \tag{52}$$

$$\mathcal{L}\left[g_m(x)-\chi_m g_{m-1}(x)\right]=Exp[-\eta]\hbar R_m(\vec{g}_{m-1}), \tag{53}$$

subject to initial conditions:

$$f_m=0,\ f'_m=0,\ \theta_m=0\ \ g'_m=0\quad \text{at}:\ \eta=0;$$
$$f'_m\to 0,\ \theta_m\to 0\quad g_m\to 0\quad \text{as:}\ \eta\to\infty, \tag{54}$$

Where

$$R_m(\vec{f}_{m-1})=\sum_{j=0}^{m-1}\frac{\partial^2 f_j(\eta)}{\partial\eta^2}\frac{\partial^2 f_{m-1-j}(\eta)}{\partial\eta^2}+\sum_{j=0}^{m-1}f_j(\eta)\frac{\partial^2 f_{m-1-j}(\eta)}{\partial\eta^2}-\frac{\partial^3 f_{m-1}(\eta)}{\partial\eta^3}$$
$$+k_1\left(2\sum_{j=0}^{m-1}\frac{\partial f_j(\eta)}{\partial\eta}\frac{\partial^3 f_{m-1-j}(\eta)}{\partial\eta^3}-\sum_{j=0}^{m-1}f_j(\eta)\frac{\partial^4 f_{m-1-j}(\eta)}{\partial\eta^4}-\sum_{j=0}^{m-1}\frac{\partial^2 f_j(\eta)}{\partial\eta^2}\frac{\partial^2 f_{m-1-j}(\eta)}{\partial\eta^2}\right)$$
$$-(Q+Da^{-1})f_{m-1}(\eta)+Gr\,\theta_{m-1}(\eta), \tag{55}$$

$$R_m(\vec{\theta}_{m-1})=(1+N_R)\frac{\partial^2\theta_{m-1}(\eta)}{\partial\eta^2}+\frac{Pr}{\beta}(1-Exp[-\beta\eta])\frac{\partial\theta_{m-1}(\eta)}{\partial\eta}$$
$$+Pr(2Exp[-\beta\eta]-\alpha)\theta_{m-1}(\eta)+Pr\ E\ \beta^2\ Exp[-2\beta\eta], \tag{56}$$

$$R_m(\vec{\theta}_{m-1}) = (1+N_R)\frac{\partial^2\theta_{m-1}(\eta)}{\partial\eta^2} + \frac{Pr}{\beta}(1-Exp[-\beta\eta])\frac{\partial\theta_{m-1}(\eta)}{\partial\eta} + Pr(2Exp[-\beta\eta]-\alpha)\theta_{m-1}(\eta) + Pr\ E\ \beta^2\ Exp[-2\beta\eta], \tag{57}$$

Evidently the solution of the mth-order deformation equations (51), (52) and (53) for $m \geq 1$ takes the form:

$$f_m(\eta) = f_{m-1}(\eta) + Exp[-\eta]\hbar\,\mathcal{L}^{-1}\left[R_m(\vec{f}_{m-1})\right], \tag{58}$$

$$\theta_m(\eta) = \theta_{m-1}(\eta) + Exp[-\eta]\hbar\,\mathcal{L}^{-1}\left[R_m(\vec{\theta}_{m-1})\right], \tag{59}$$

$$g_m(\eta) = g_{m-1}(\eta) + Exp[-\eta]\hbar\,\mathcal{L}^{-1}\left[R_m(\vec{g}_{m-1})\right], \tag{60}$$

5 RESULTS AND DISCUSSION

We employed several terms in evaluating the approximate solution $f_{a\,pp} = \sum_{i=0}^{n} f_i$, $\theta_{a\,pp} = \sum_{i=0}^{n}\theta_i$, $g_{a\,pp} = \sum_{i=0}^{n} g_i$, and highlight that the solution series contains the auxiliary parameter $\hbar$ - this facilitates the control of the convergence of the series solution, via the so-called $\hbar$-curve i.e., a curve of a versus $\hbar$. As pointed by Liao (2003), the valid region of $\hbar$ is a horizontal line segment. Figures 2 and 3 show the $\hbar$-curve for various orders of HAM. These curves reveal that when the order of series is 20 the segment of horizontal line is in excess of the other orders. To establish the range of admissible values of $\hbar$, a $\hbar$-curve for each $f''(0)$ and $\theta'(0)$ obtained by the 20th-order HAM approximation are plotted in Figures 4 and 5, with various values of Q respectively. From these figures, the valid regions of $\hbar$ correspond to the line segments nearly parallel to the horizontal axis. We can select the best value of $\hbar$ from the residual curves (Figures 6 and 7), which has a minimum range of $R_{20}(\vec{f})$ or $R_{20}(\vec{\theta})$, $vis-a-vis\ \eta$. It is evident that $\hbar = -0.4$ has the minimum range on the residual-curve. A default value of Da = 1 is used throughout corresponding to a highly permeable regime. Also unless otherwise specified we take $k_1 = 0.2$, $\alpha = 0$, $E = 0.25$, $Pr = 4$ and $N_R = 1$. We have compared our results with those of numerical method based on shooting quadrature and a 4th order Runge-Kutta solver. Figure 8 and Table 1 compare the analytical and the numerical solution for the dimensionless velocity, f'. Figure 9 depicts the results for the dimensionless temperature θ, for various values of Q respectively. Generally excellent correlation is achieved between the HAM and numerical results.

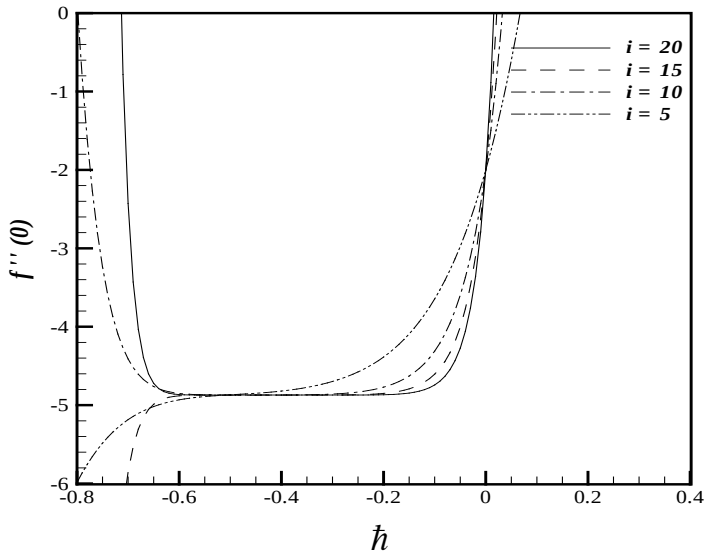

Figure 2: The $\hbar$ curve of $f''(0)$ given by various order approximate solution, when $Q = 1$ and $k_1 = 0.2$.

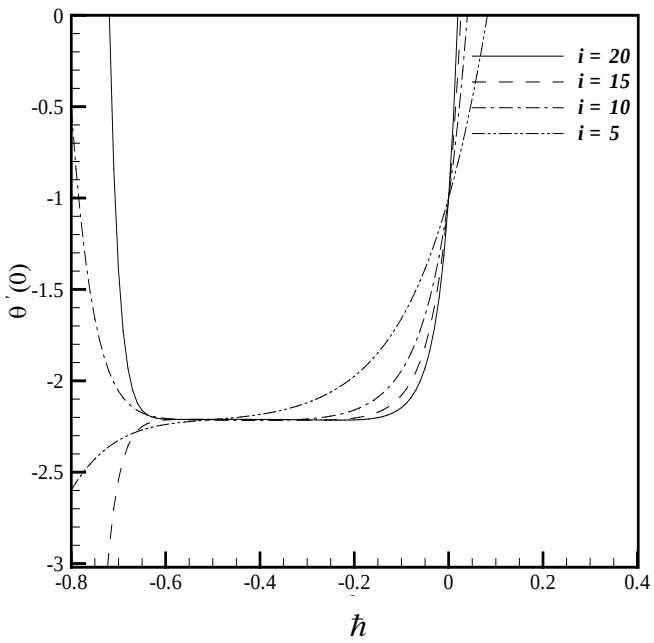

Figure 3: The $\hbar$-*curve* of $\theta'(0)$ given by various order approximate solution, when $Q = 1,\ k_1 = 0.2,\ \alpha = 0,\ E = 0.25,\ Pr = 4$ and $N_R = 1$.

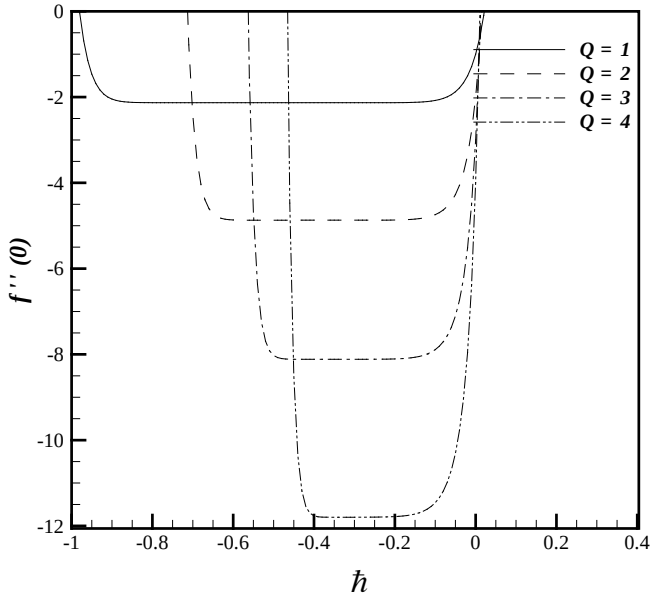

Figure 4: The $\hbar$-*curve* of $f''(0)$ given by 20th-order HAM solution for various values of Q, when $k_1 = 0.2,\ \alpha = 0,\ E = 0.25,\ Pr = 4$ and $N_R = 1$.

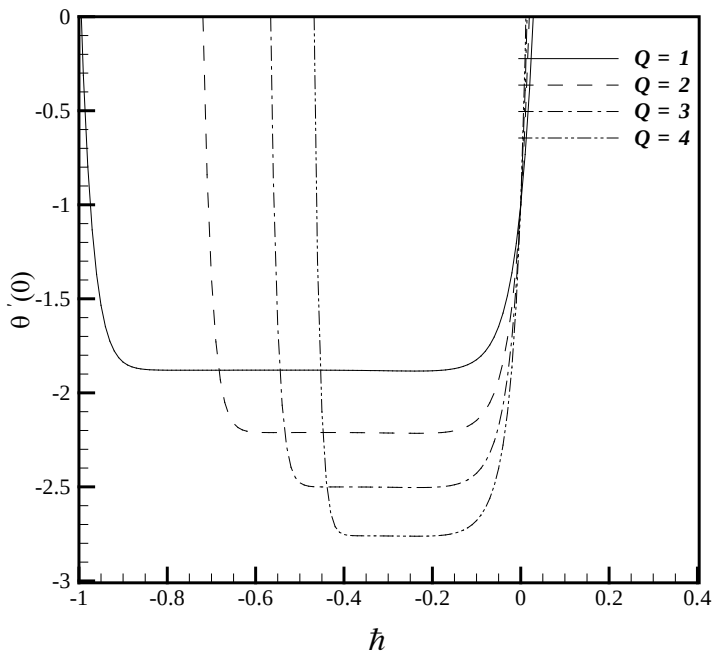

Figure 5: The $\hbar$-*curve* of $\theta'(0)$ given by 20th-order HAM solution for various values of Q, when $k_1 = 0.2,\ \alpha = 0,\ E = 0.25,\ Pr = 4$ and $N_R = 1$.

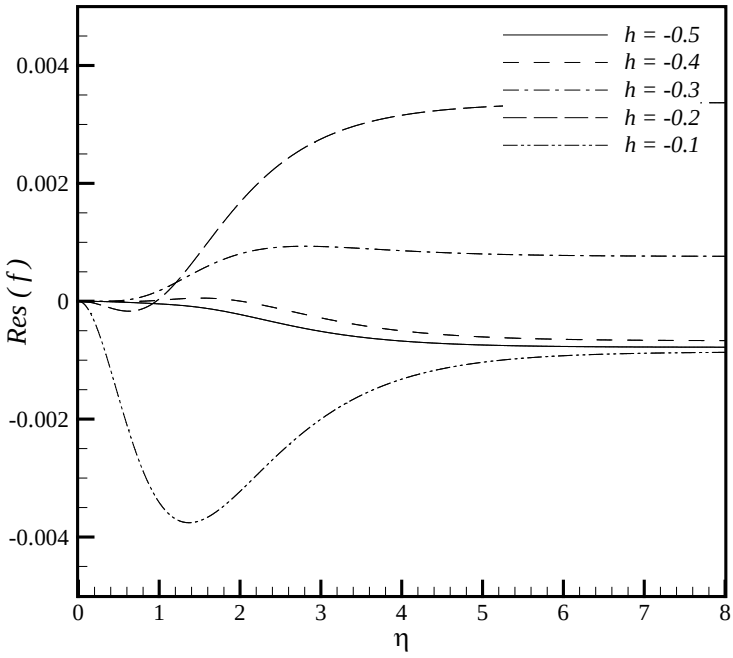

Figure 6: The behavior of the solutions $Re_{20}(f)$ obtained by the HAM for various $\hbar$ when $Q=1,\ k_1=0.2,\ \alpha=0,\ E=0.25,\ Pr=4$ and $N_R=1$.

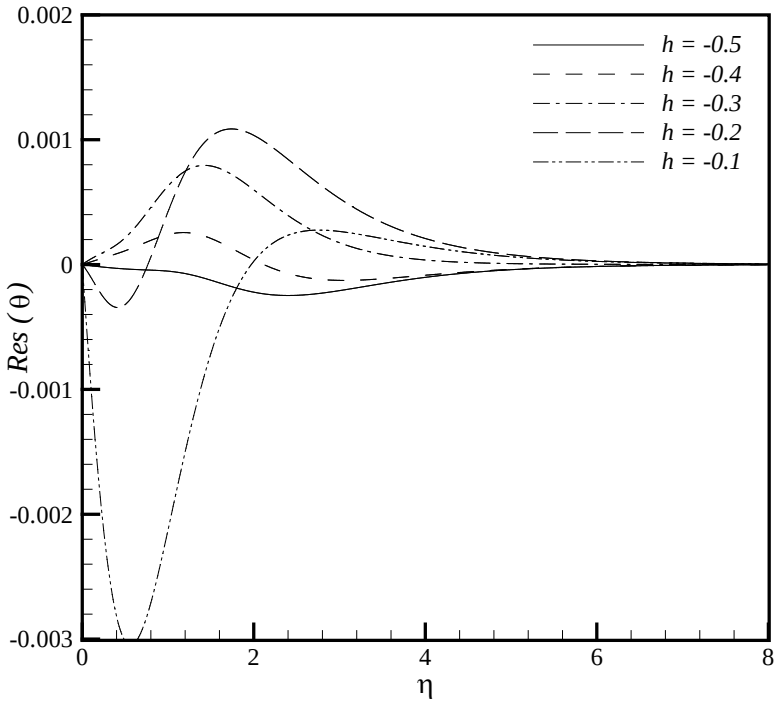

Figure 7: The behavior of the solutions $Re_{20}(\theta)$ obtained by the HAM for various $\hbar$ when $Q=1,\ k_1=0.2,\ \alpha=0,\ E=0.25,\ Pr=4$ and $N_R=1$.

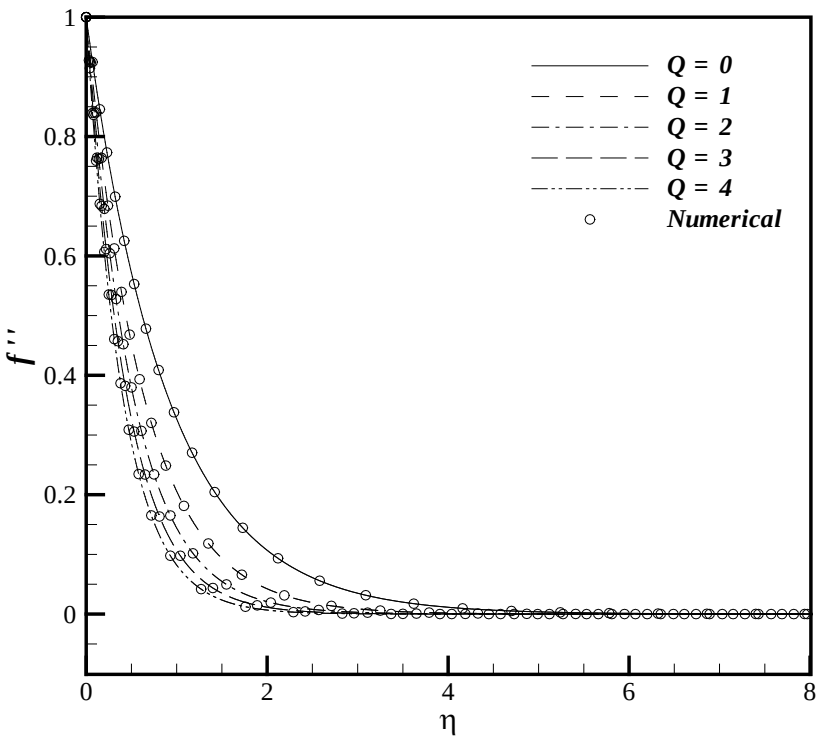

Figure 8: Comparison between numerical quadrature and HAM for $f'(\eta)$ with various values of Q, when $k_1 = 0.2$, $\alpha = 0$, $E = 0.25$, $Pr = 4$, $N_R = 1$, and $\hbar = -0.4$.

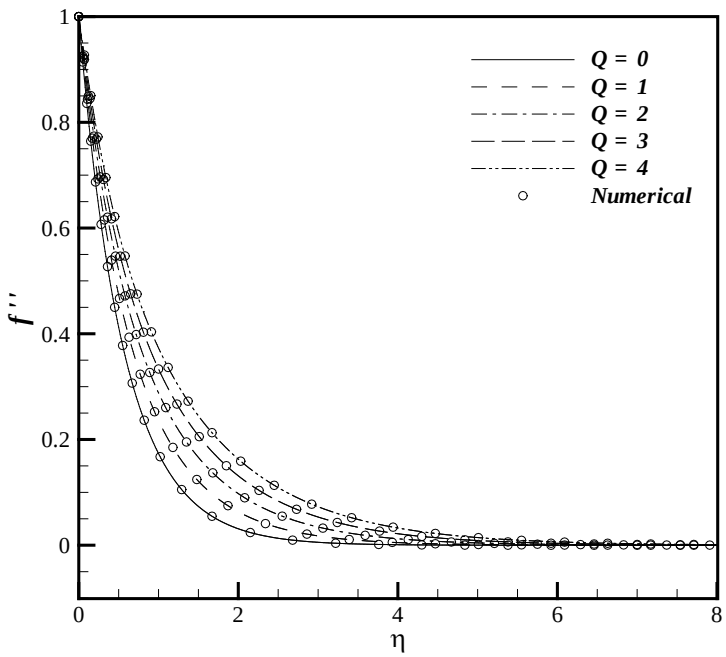

Figure 9: Comparison between the numerical quadrature and HAM for $\theta(\eta)$ with various values of Q, when $k_1 = 0.2$, $\alpha = 0$, $E = 0.25$, $Pr = 4$, $N_R = 1$, and $\hbar = -0.4$.

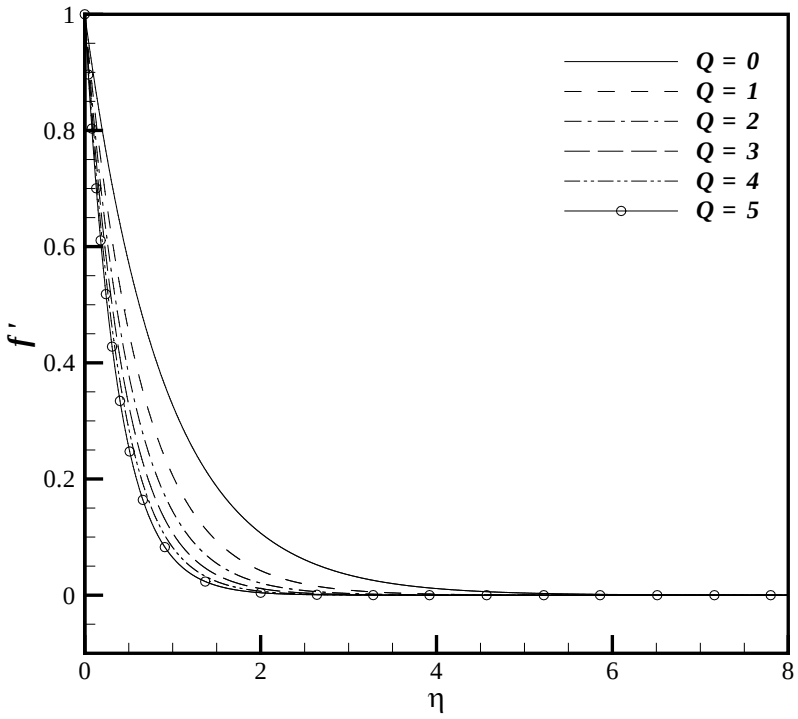

Figure 10: Velocity profiles, $f'(\eta)$ obtained by HAM for various values of Q, when $k_1 = 0.2,\ \alpha = 0,\ E = 0.25,\ Pr = 4$ and $N_R = 1$.

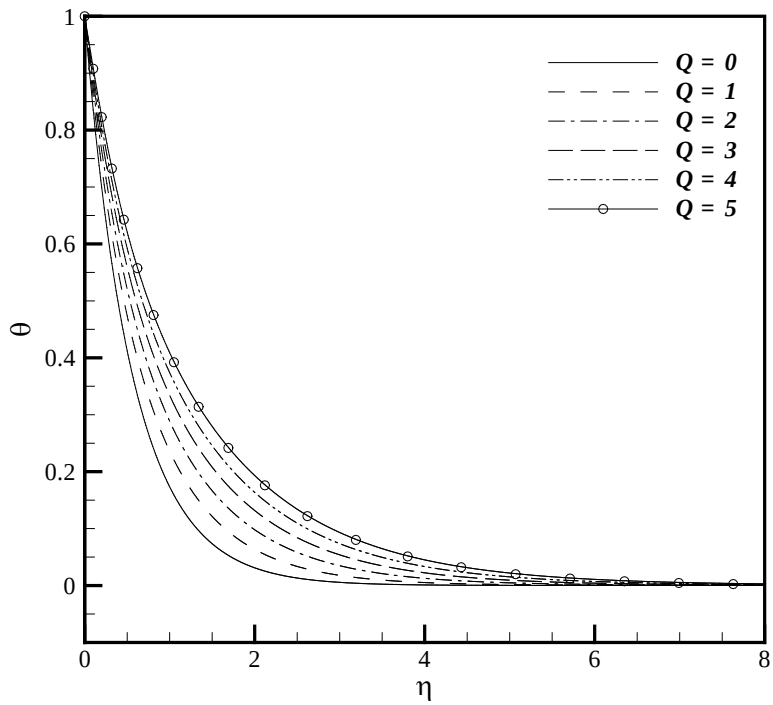

Figure 11: Temperature profiles, $\theta(\eta)$ obtained by HAM for various values of Q, when $k_1 = 0.2,\ \alpha = 0,\ E = 0.25,\ Pr = 4$ and $N_R = 1$ (PST case).

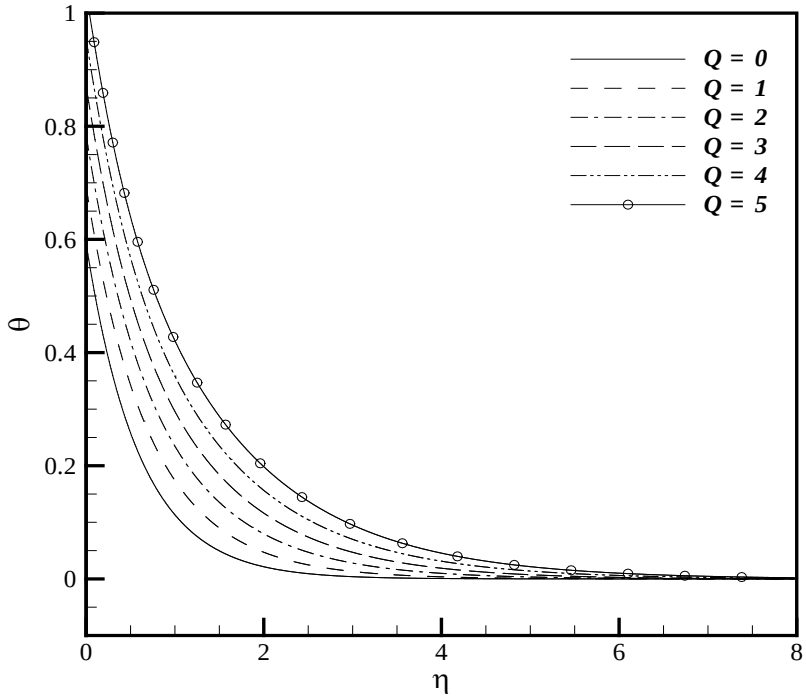

Figure 12: Temperature profiles, $g(\eta)$ obtained by the HAM for various values of Q, when $k_1 = 0.2,\ \alpha = 0,\ E = 0.25,\ Pr = 4$ and $N_R = 1$ (PHF case).

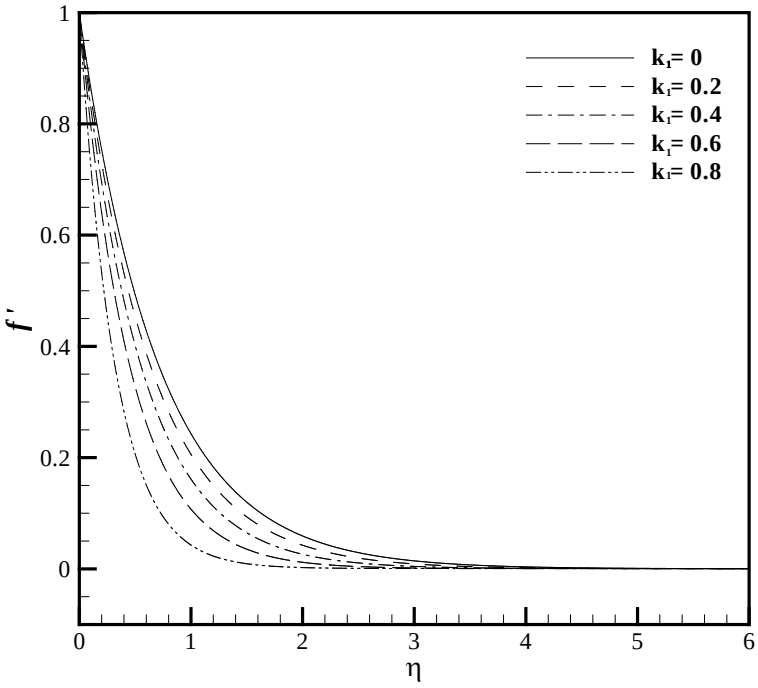

Figure 13: Velocity profiles, $f'(\eta)$ obtained by the HAM for various values of k_1, when $Q = 1,\ \alpha = 0,\ E = 0.25,\ Pr = 4$ and $N_R = 1$.

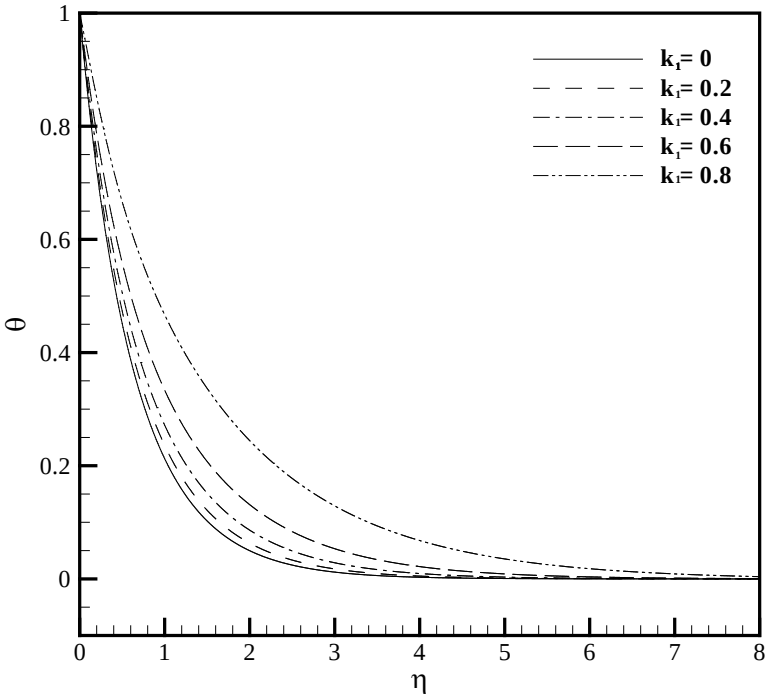

Figure 14: Temperature profiles, $\theta(\eta)$ obtained by the HAM for various values of k_1, when $Q = 1, \alpha = 0, E = 0.25, Pr = 4$ and $N_R = 1$ (PST case).

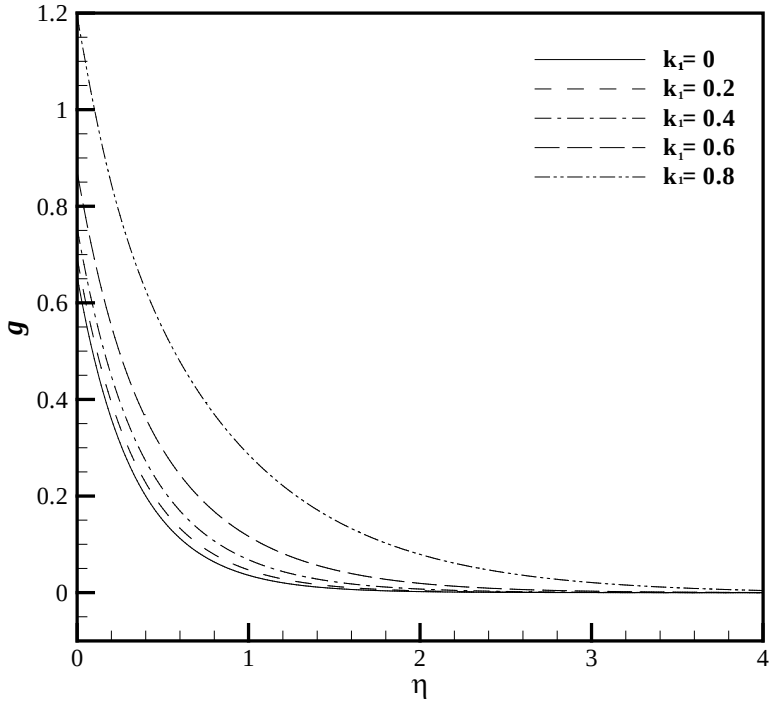

Figure 15: Temperature profiles, $g(\eta)$ obtained by the HAM for various values of k_1, when $Q = 1, \alpha = 0, E = 0.25, Pr = 4$ and $N_R = 1$ (PHF case).

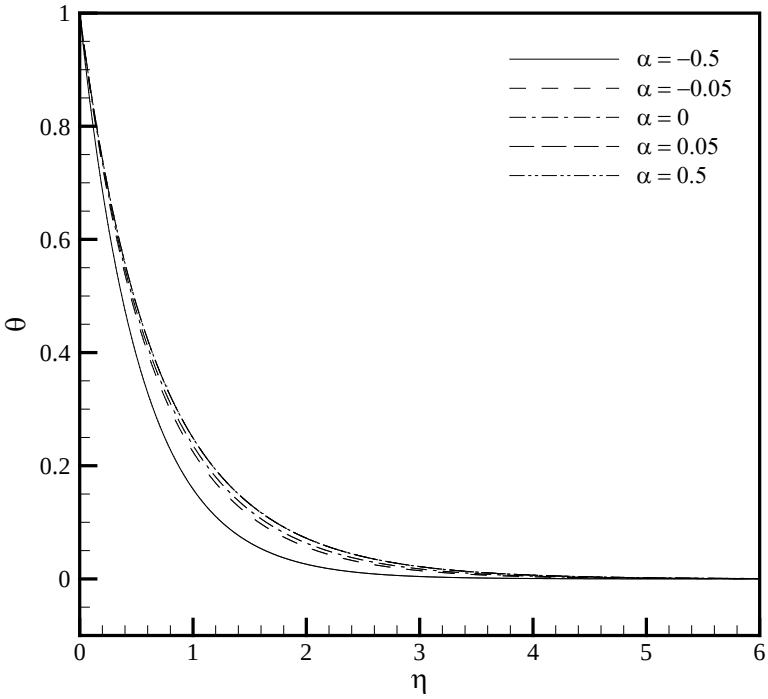

Figure 16: Temperature profiles, $\theta(\eta)$ obtained by the HAM for various values of α when $Q = 1$, $k_1 = 0.2$, $E = 0.25$, $Pr = 4$ and $N_R = 1$ (PST case).

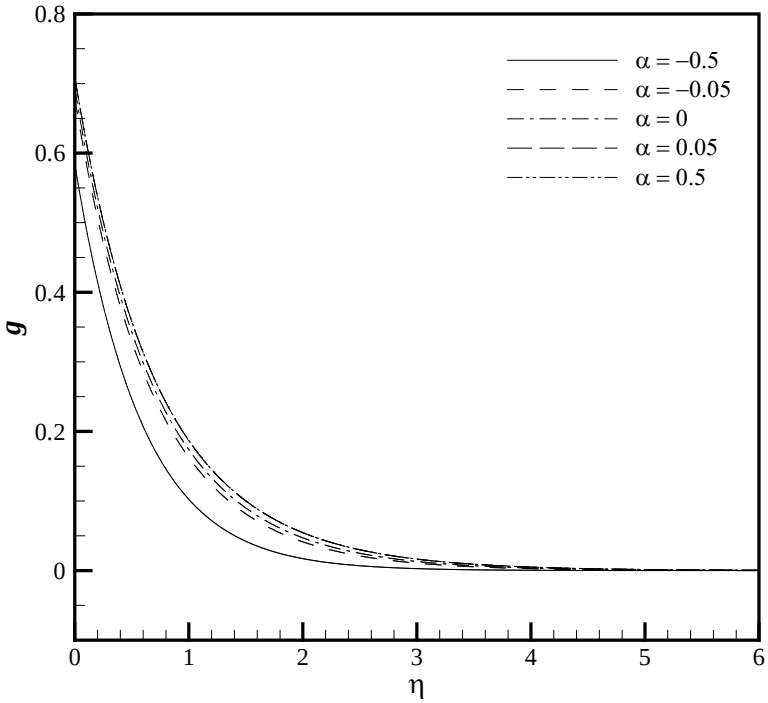

Figure 17: Temperature profiles, $g(\eta)$ obtained by the HAM for various values of α when $Q = 1$, $k_1 = 0.2$, $E = 0.25$, $Pr = 4$ and $N_R = 1$ (PHF case).

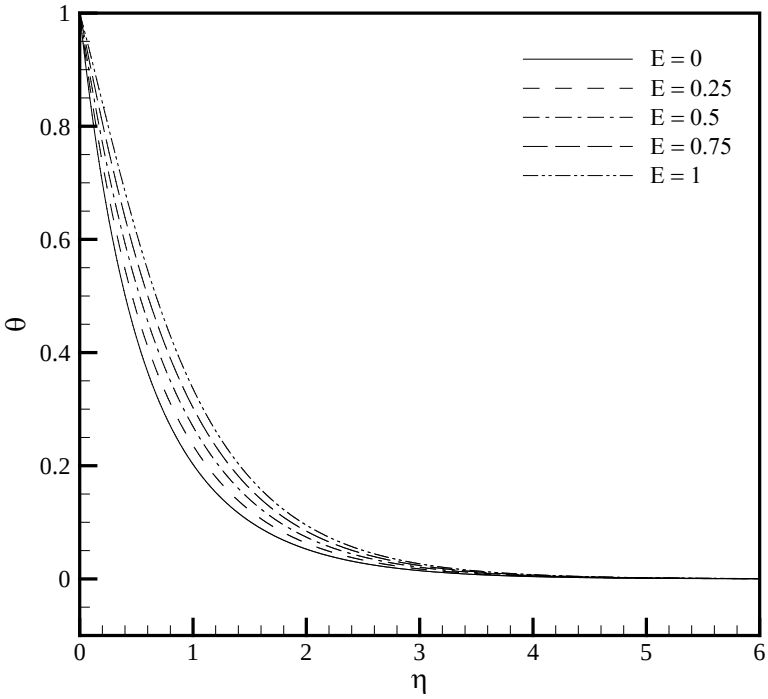

Figure 18: Temperature profiles, $\theta(\eta)$ obtained by the HAM for various values of E when $Q = 1$, $k_1 = 0.2$, $\alpha = 0$, $Pr = 4$ and $N_R = 1$ (PST case).

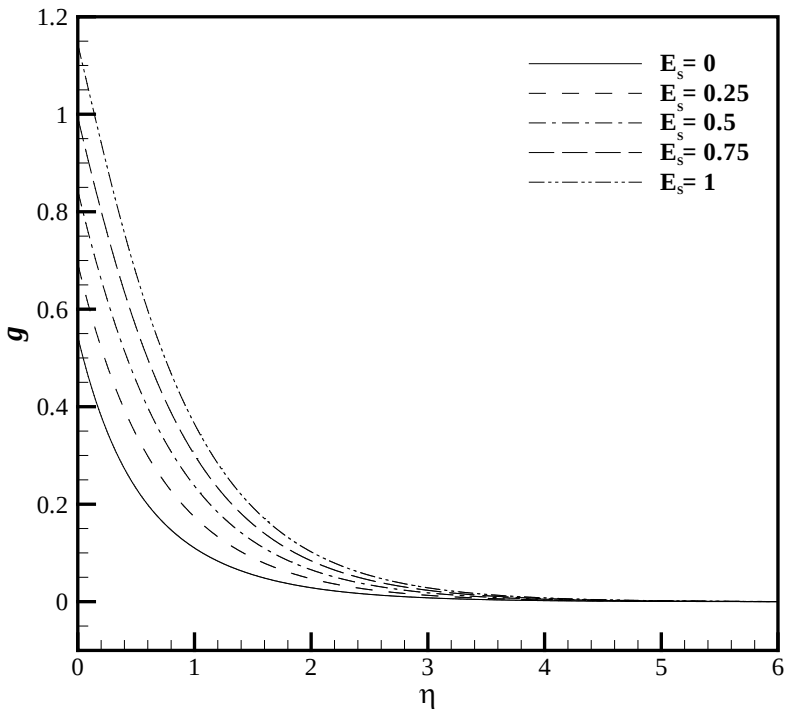

Figure 19: Temperature profiles, $g(\eta)$ obtained by the HAM for various values of E_S when $Q = 1$, $k_1 = 0.2$, $\alpha = 0$, $Pr = 4$ and $N_R = 1$ (PHF case).

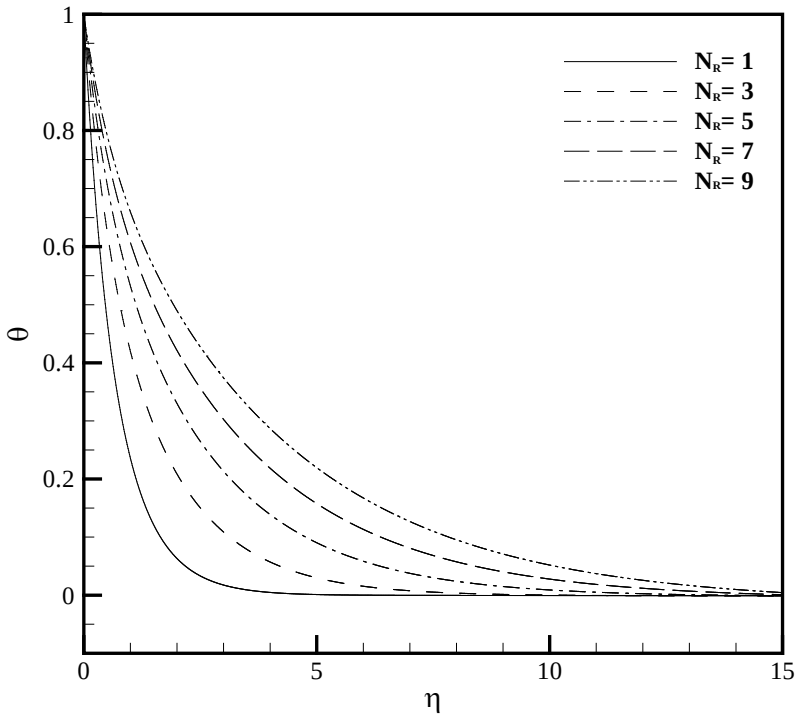

Figure 20: Temperature profiles, $\theta(\eta)$ obtained by the HAM for various values of N_R when $Q = 1,\ k_1 = 0.2,\ \alpha = 0,\ Pr = 4$ and $E = 0.25$ (PST case).

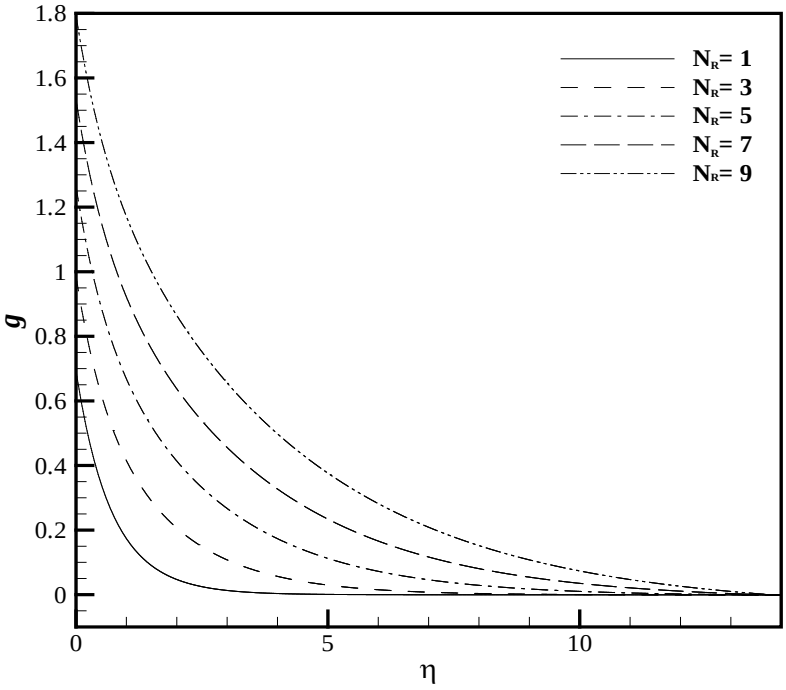

Figure 21: Temperature profiles, $g(\eta)$ obtained by the HAM for various values of N_R when $Q = 1,\ k_1 = 0.2,\ \alpha = 0,\ Pr = 4$ and $E_S = 0.25$ (PHF case).

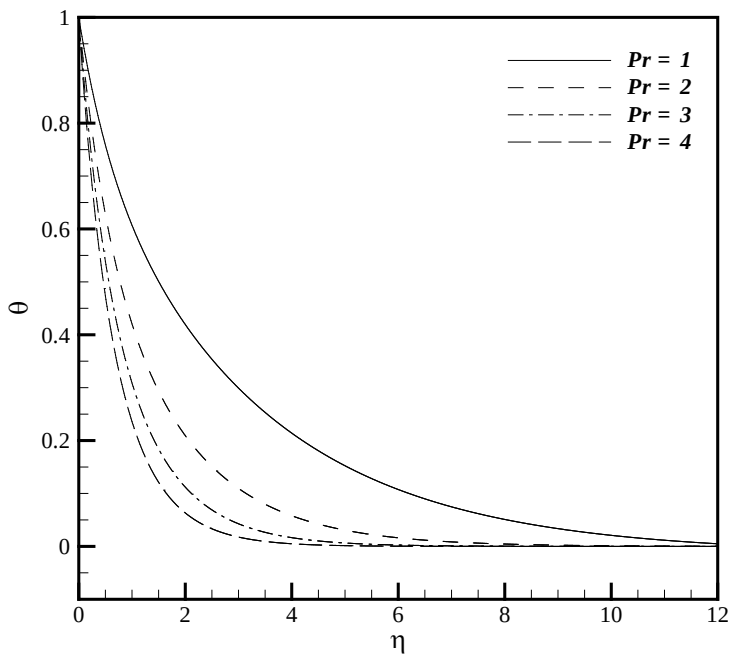

Figure 22: Temperature profiles, $\theta(\eta)$ obtained by the HAM for various values of Pr when $Q = 1,\ k_1 = 0.2,\ \alpha = 0,\ E = 0.25$ and $N_R = 1$ (PST case).

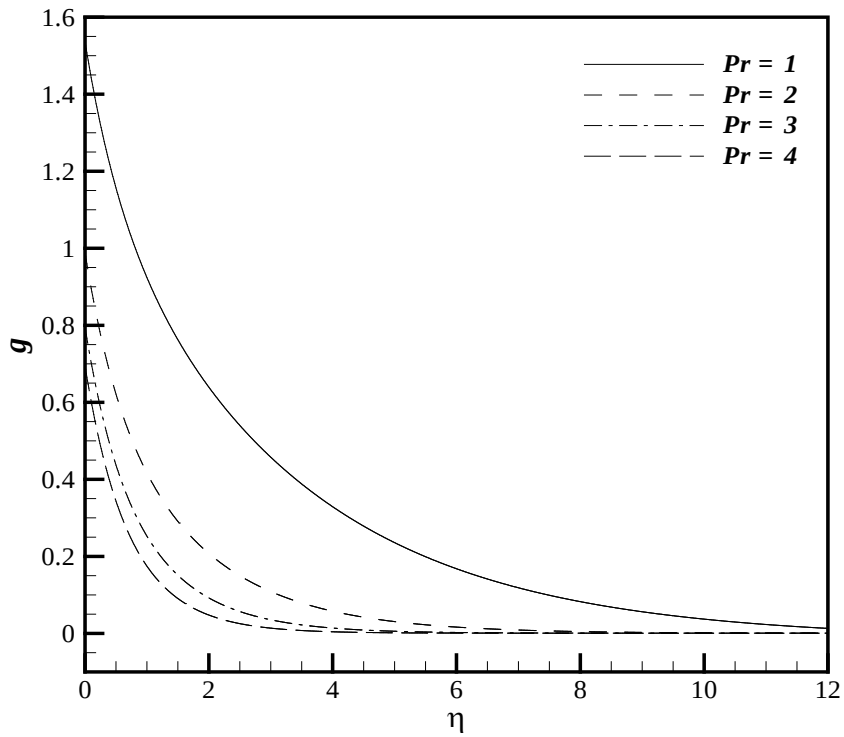

Figure 23: Temperature profiles, $g(\eta)$ obtained by the HAM for various values of Pr when $Q = 1,\ k_1 = 0.2,\ \alpha = 0,\ E_S = 0.25$ and $N_R = 1$ (PHF case).

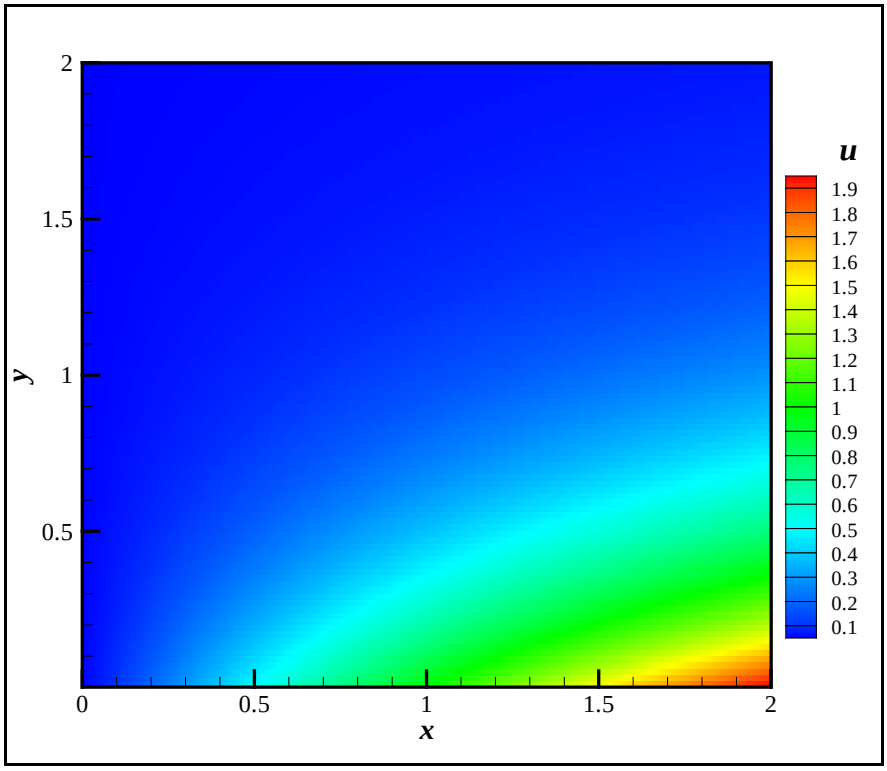

Figure 24: Velocity component along the sheet contour, when $Q = 2,\ k_1 = 0.2,\ \alpha = 0,\ E = 0.25,\ Pr = 4$ and $N_R = 1$.

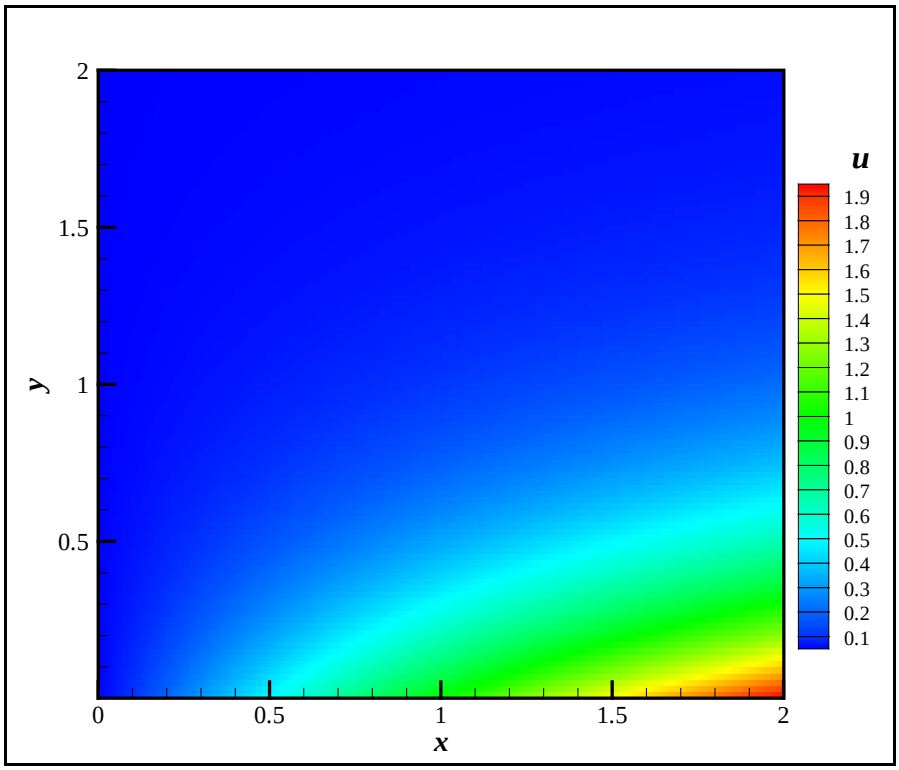

Figure 25: Velocity component along the sheet contour, when $Q = 3,\ k_1 = 0.2,\ \alpha = 0,\ E = 0.25,\ Pr = 4$ and $N_R = 1$.

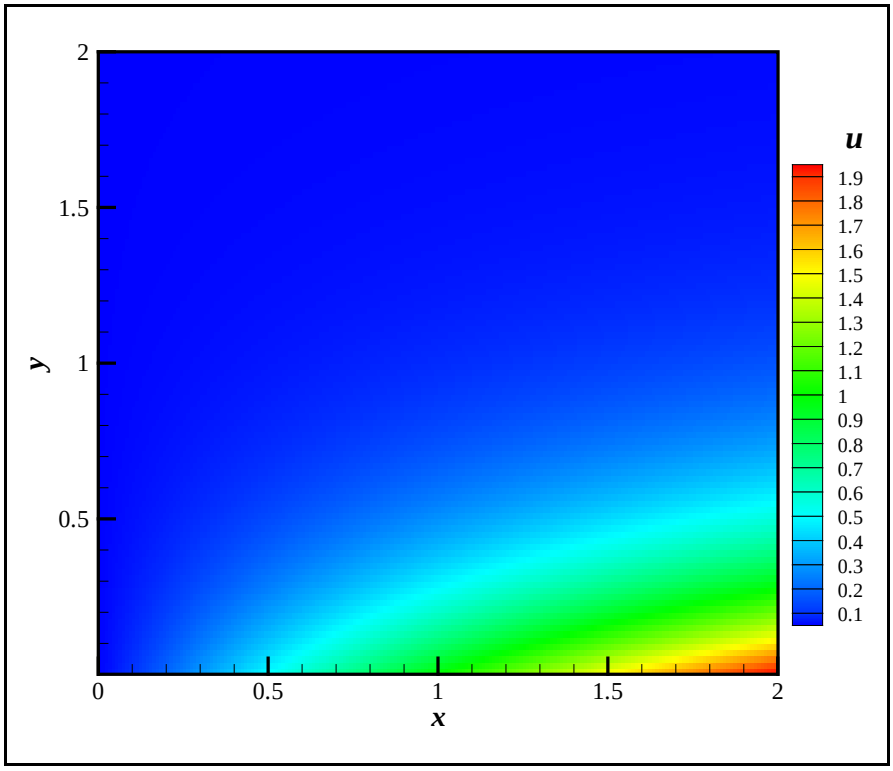

Figure 26: Velocity component along the sheet contour, when $Q = 4,\ k_1 = 0.2,\ \alpha = 0,\ E = 0.25,\ Pr = 4$ and $N_R = 1$.

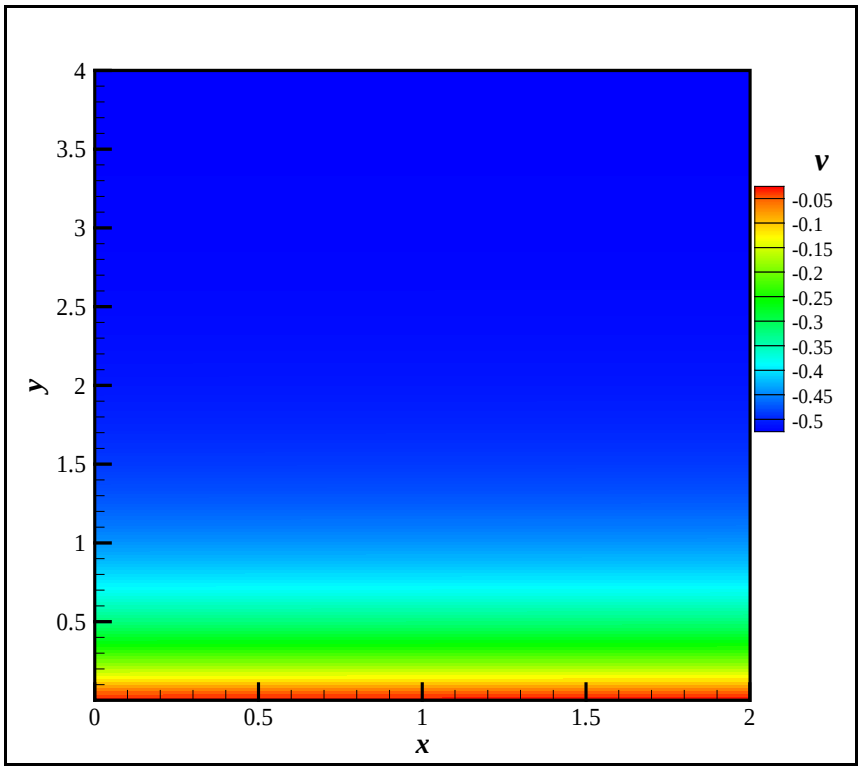

Figure 27: Velocity component normal to the sheet contour, when $Q = 2,\ k_1 = 0.2,\ \alpha = 0,\ E = 0.25,\ Pr = 4$ and $N_R = 1$.

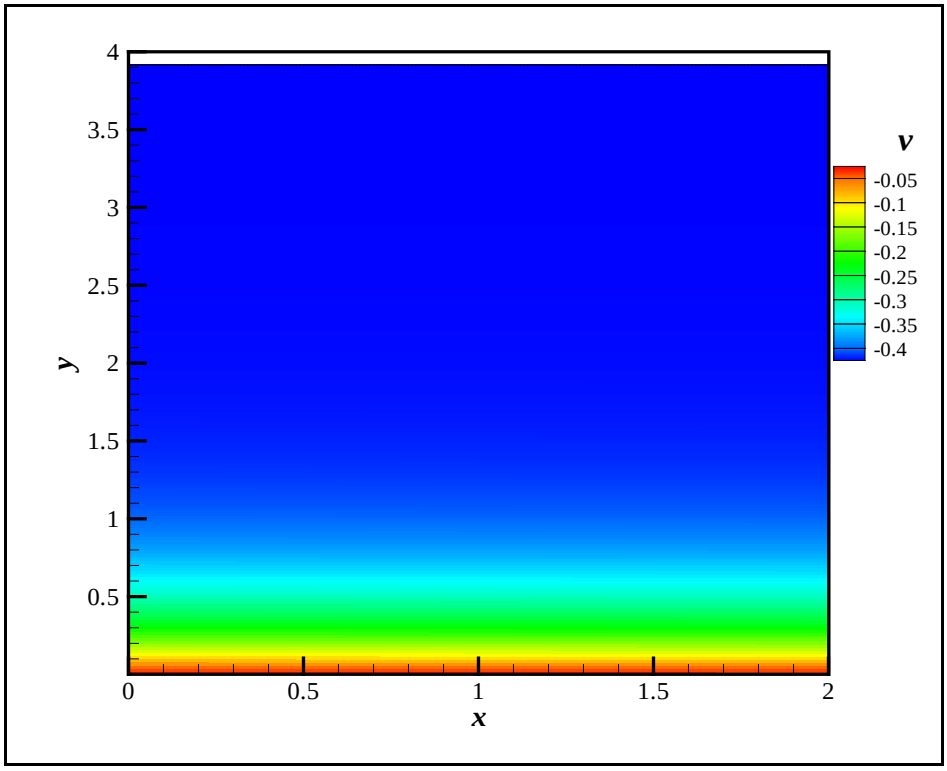

Figure 28: Velocity component normal to the sheet contour, when $Q = 3,\ k_1 = 0.2,\ \alpha = 0,\ E = 0.25,\ Pr = 4$ and $N_R = 1$.

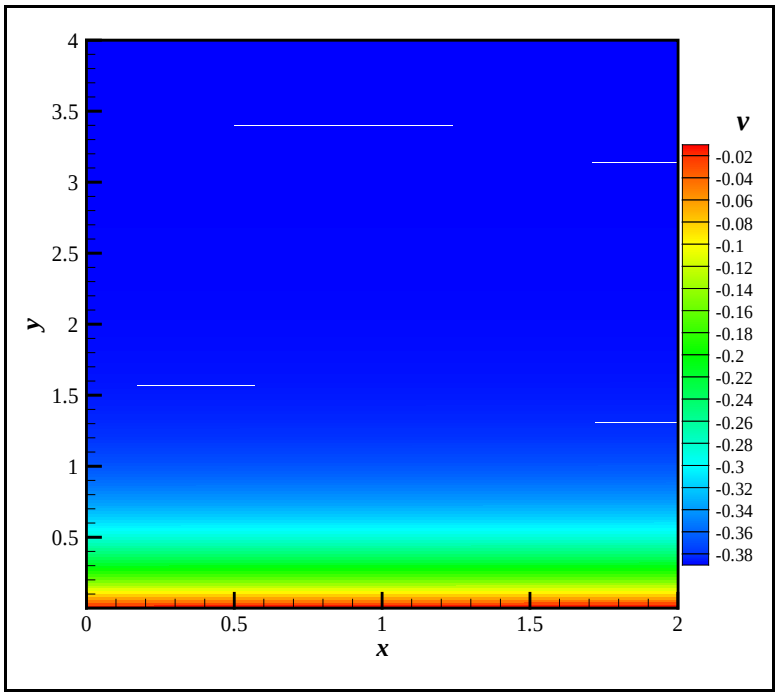

Figure 29: Velocity component normal to the sheet contour, when $Q = 4,\ k_1 = 0.2,\ \alpha = 0,\ E = 0.25,\ Pr = 4$ and $N_R = 1$.

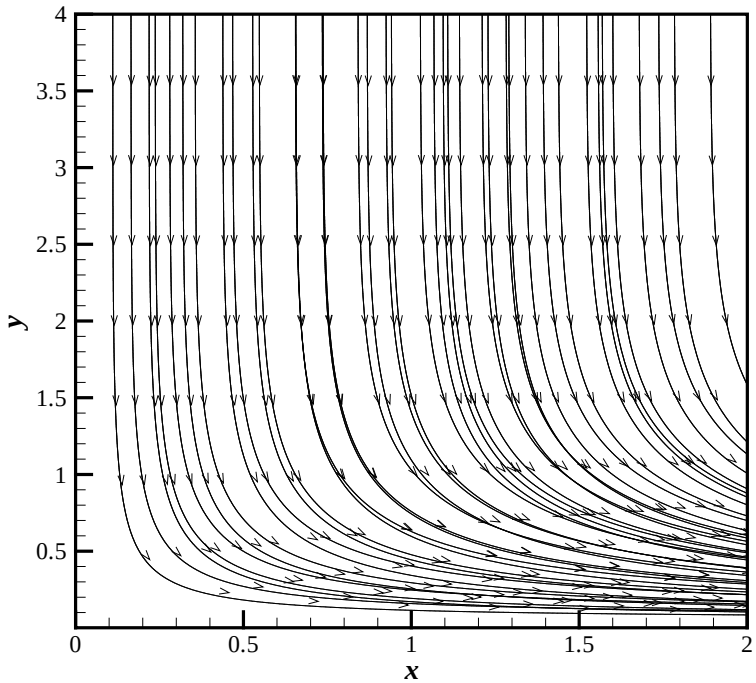

Figure 30: Vector analysis, when $Q = 2$, $k_1 = 0.2$, $\alpha = 0$, $E = 0.25$, $Pr = 4$ and $N_R = 1$.

Figures 10-12 illustrate the effect of the magnetic parameter, Chandrasekhar number (Q), on the dimensionless velocity, $f'(\eta)$ and the PST case temperature, $\theta(\eta)$ and PHF case temperature, $g(\eta)$. Q is the square of the Hartmann number, $\left(B_0\sqrt{\frac{\sigma}{b\,\rho}}\right)$. It is therefore directly proportional to the square of the applied magnetic field, B_0. This parameter arises in the Lorentzian transverse magnetic drag term, Q f_η in the momentum similarity equation (5), where f_η i.e. $f^{/}$ is the velocity. It acts to strongly retard the flow along the x-direction and control the stretching of the sheet. This is indeed testified to by figure 10 where we observe a considerable reduction in flow velocity as Q rises from 0 (non-conducting case) to 5. We further note that with stronger magnetic field, the velocity decay from the wall evolves from a gradual montonic decay (Q = 0) to a very steep descent close to the sheet surface. Flow development in the boundary layer is therefore curtailed significantly with imposition of progressively stronger magnetic field. = In figure 11, the reverse effect is generated in the PST temperature field. Increasing Q effectively enhances temperatures in the boundary layer. As elucidated in Abel and Nandeppanavar (2007, 2008a,b) and further confirmed by Bég et al. (2011d), the supplementary work done to drag the viscoelastic fluid against the action of the magnetic field, manifests as a dissipation in thermal energy. These patterns were originally identified by Rossow (1958) in laminar boundary layer hydromagnetic, but for Newtonian fluids only. It also arises clearly for viscoelastic flows. This elevates the temperature in the boundary layer. A similar response is observed for the PST temperature field, in figure 12. However it is evident that in figure 12 a single wall temperature (at η = 0) for the different profiles does not feature- the initial temperature at the wall varies in each profile, since the

heat flux is prescribed in this scenario, not the surface temperature. = The potent effect of magnetic field is however clearly observed and again serves to heat the fluid in the boundary layer.

Figures 13-15 depict the influence of the viscoelastic parameter (k_1) on velocity and PST and PHF temperature profiles. This parameter again only arises in the momentum equation (5). It is inversely proportional to the dynamic viscosity of the liquid and directly proportional to the viscoelastic dimensional parameter, k_0. Increasing k_1 induces a strong depression in the velocity i.e. decelerates the flow. This physically generates greater tensile stresses (elongational) in the fluid which is a primary mechanism contributing to the retardation (Bég et al, 2011d). Since the fluid flow slower, thermal diffusion becomes more dominant in the boundary layer convection regime. This acts to accentuate temperatures. In consistency with these physical arguments, inspection of figures 13 to 15 shows that $f'(\eta)$ is clearly decreased and values of $\theta(\eta)$ and $g(\eta)$ are strongly increased with a rise in viscoelasticity parameter, (k_1). A similar response for other viscoelastic fluid models has been reported quite recently also by Husain et al. (2008) for Oldroyd-B fluids and Hayat and Abbas (2008 for the second-order differential non-Newtonian fluid. The strong coupling of the velocity and thermal fields via eqn. (5) and equation (15) or equation (28) implies that the viscoelasticity effect while absent in temperature equations, still exerts a very prominent role on the transport of heat in the boundary layer. Finally we note that the case, $k_1 = 0$ implies a Newtonian fluid and for this scenario the temperatures are minimized in the boundary layer, while the velocity is maximized.

Figures 16 and 17 display the influence of the heat source/sink parameter (α) on $\theta(\eta)$ and $g(\eta)$. $\alpha > 0$ corresponds to a heat source (generation of thermal energy) and $\alpha < 0$ to a heat sink (destruction of thermal energy). With $\alpha > 0$ both temperature profiles are markedly elevated; the reverse is clearly observed for the heat sink effect ($\alpha < 0$). A similar response has also been reported in magneto-micropolar = convection flow using the finite element method by Rawat et al. (2009).

Figures 18 and 19 show the response of the PST temperature and PHF temperature profiles, to a change in Eckert number, E and re-scaled Eckert number, E_s, respectively. E and Es express the relationship between the kinetic energy in the flow and the enthalpy. It signifies the conversion of kinetic energy into internal energy by work done against the viscous fluid stresses. Although this parameter is often used in supersonic aerodynamics (compressible) flow, it has significance in high temperature incompressible flows, as typified by materials processing operations. Positive Eckert number implies cooling of the stretching sheet and therefore a transfer of heat to the fluid. Convection is enhanced and we observe in consistency with this that both temperature profiles are significantly boosted with increasing E and E_s, respectively. Viscous dissipation therefore exerts a major role on the temperature distribution in the regime.

Figures 20 and 21 illustrate the effect of the radiation-conduction number on temperature profiles

for the PST case and PHF case. Nr = $\left(\frac{16\sigma^* T_\infty^3}{3k\,k^*}\right)$ embodies the relative contribution of heat transfer by thermal radiation to thermal conduction. Large Nr (>1) values therefore

correspond to thermal radiation dominance and small values (<1) to thermal conduction dominance. For Nr = 1 both conduction and radiative heat transfer modes will contribute equally to the regime. Thermal radiation serves to augment the diffusion term in the energy equation (15) or (28). For Nr = 0, thermal radiation vanishes. With an increase in Nr i.e. stronger thermal radiation flux, from 1 through to 9, there is an accompanying elevation in temperatures in both figures 20 and 21. Radiative flux therefore contributes considerable thermal energy to the boundary layer regime.

Figures 22 and 23 show the influence of Prandtl number (Pr) on both PST and PHF temperature profiles. Larger Pr values imply a thinner thermal boundary layer thickness and more uniform temperature distributions across the boundary layer. Hence the thermal boundary layer will be much less in thickness than the hydrodynamic (translational velocity) boundary layer. Pr = 1 implies that the thermal and velocity boundary layers are approximately equal in extent. Smaller Pr fluids have higher thermal conductivities so that heat can diffuse away from the vertical surface faster than for higher Pr fluids (thicker boundary layers). In accordance with this, a strong decrease in temperature accompanies an increase in Prandtl number in both figures 22 and 23.

Figures 24-26 and figures 27-29, illustrate respectively the contours of the velocity component along the sheet and normal to the sheet, for various values of Q. Inspection of the figures confirms that the magnetic parameter, Q, exerts a decelerating effect on the flow. The magnitudes of the x-direction velocity, u, are clearly suppressed with a rise in Q from 2, 3 to 4. A similar response is observed in the transverse velocity component, v, where again the magnitudes are significantly reduced with increasing strength of magnetic field i.e. higher Q. The powerful inhibiting mechanism of an applied magnetic field transverse to a stretching sheet is therefore strongly confirmed form figures 24 to 29.
Finally in figure 30, we have plotted the x-y contours for velocity. The clustering of vectors around the x axis indicates the presence of an inhibiting effect due to magnetic field. Flow vectors converge towards the lower right hand corner of the diagram. Table 1 documents numerical values of velocity $f^{/}$, with increasing Q values as computed by both numerical quadrature and HAM. Reading across the table, it is immediately apparent that increasing Chandrasekhar number clearly decreases velocities i.e. decelerates the flow. The excellent correlation between HAM and numerical shooting solutions once again strongly advocates the robustness of HAM in chemical engineering fluid flow simulations.

Table1: Comparison of $f\ '(\eta)$ obtained by the HAM solution with numerical values for $k_1 = 0.2$ with various values of Q.

η	$f\ '(\eta)$ obtained by the HAM					
	$Q = 2$		$Q = 3$		$Q = 4$	
	Numerical	HAM	Numerical	HAM	Numerical	HAM
0.5	0.379749	0.379742	0.326922	0.326917	0.286505	0.286501
1.5	0.0547632	0.0547605	0.0349407	0.0349393	0.0235177	0.0235169
2.5	0.00789734	0.0078967	0.00373439	0.00373413	0.00193045	0.00193033
3.5	0.00113887	0.00113874	0.000399124	0.000399085	0.000158461	0.000158447

6 CONCLUSIONS

The present article has analyzed in detail using a hypergeometric analytical method, the semi-numerical homotopy analysis method (HAM) and also numerical quadrature, the radiative-convective magnetohydrodynamic viscoelastic flow along a stretching sheet in a porous medium. Heat source/sink effects have also been studied. Two thermal cases have been studied for the stretching sheet - a prescribed surface temperature and also a prescribed heat flux. The computations have shown for a fixed permeability of the regime (Darcy number of unity) that:

(i) Increasing magnetic field (Q) serves to retard the flow in the regime but to enhance temperatures.

(ii) increasing viscoelasticity (k_0) acts to decelerate the flow and to elevate temperatures

(iii) increasing Prandtl number (Pr) depresses temperatures

(iv) increasing Eckert numbers (E, E_s) enhances significantly temperatures

(v) Increasing radiation-conduction number (N_R) boosts the temperatures through the boundary layer

(vi) Increasing heat source parameter (α >0) elevates temperatures with the converse behaviour induced with an increase in heat sink strength (α <0).

The present study has also further endorsed the excellent potential of HAM in modern multi-physical magnetic materials processing and demonstrates that this approach is a very useful tool for nonlinear viscous fluid dynamics, and a new procedure for validating traditional (finite difference, finite element) numerical codes. HAM provides a convenient way to control the convergence of approximate series, which is a fundamental qualitative difference between this technique and other traditional perturbation methods. This method does not require a small parameter in any equation as is customary with perturbation methods as employed by modern chemical engineers (Rice and Do, 1994). The authors are currently exploring HAM simulation in other nonlinear chemo-fluid dynamics problems involving surface tension effects (Marangoni convection) (Zueco and Bég, 2011), chemical reaction (Cortell, 2007) and rotational body force (Bég et al. 2008b) effects - the results of these investigations will be communicated imminently.

7 ACKNOWLEDGMENTS

MM Rashidi acknowledges gratefully one year in the capacity of Invited Professor at the Université de Sherbrooke (Montreal, Canada), during 2010–2011.
The author Dr. U.S. Mahabaleshwar wishes to thank Bharat Ratna Prof. Dr. C.N.R.Rao *F.R.S*, Hon'ble Chairman VGST and Dr. S. Anant Raj, Consultant, Department of IT, BT Science & Technlogy, Government of Karnataka, India, for supporting this work under Seed Money to Young Scientists for Research (# **VGST/SMYSR/GRD-304/2013-14)**

NOMENCLATURE

A, B, D	Constants
b	Constant rate of stretching [s^{-1}]
C_P	Specific heat at constant pressure [W kg^{-1} K^{-1}]
Da	(γ/ck') Darcy number
E	$\left(\frac{b^2 l^2}{A\, C_p}\right)$ Eckert number
E_S	$\left(\frac{E}{D}\sqrt{\frac{b}{\nu}}\right)$ scaled Eckert number
f	Similarity function
F	Kummer's function
g	$\left(\frac{T - T_\infty}{T_w - T_\infty}\right)$ non- dimensional temperature (for the PHF case)
H_0	Strength of the magnetic field [w m^{-2}]
k	Thermal conductivity [W kg^{-1} K^{-1}]
$\hbar$	Auxiliary parameter
H	Auxiliary function
$\mathcal{L}$	Linear operator of the HAM
$\mathcal{N}$	Non-linear operator of the HAM
k^*	Mean absorption coefficient [m^{-2}]
k_0	Axial velocity component
k_1	$k_1 = \frac{k_0 c}{\mu}$ viscoelastic parameter
l	Characteristic length [m]
M	$\left(B_0\sqrt{\frac{\sigma}{b\,\rho}}\right)$ Hartmann number
N_R	$\left(\frac{16\sigma^* T_\infty^3}{3k\,k^*}\right)$ radiation-conduction number
Pr	$\left(\frac{\nu}{\alpha^*}\right)$ Prandtl number
q_r	Radiative heat flux [W kg^{-1} m^{-1}]
q_w	Local heat flux at the wall
Q	M^2 (Chandrasekhar hydromagnetic number)
Q^*	uniform heat source [W kg^{-1} $K^{-1}m^{-2}$]
R_m	$\left(\frac{b\,l^2}{\nu_m}\right)$ magnetic Reynolds number
s	Variable heat flux index
T	Fluid temperature [K]
T_∞	Constant temperature far away from the sheet [K]

T_w	Wall (sheet) temperature [K]
u	Velocity component along the sheet [m s^{-1}]
v	Velocity component normal to the sheet [m s^{-1}]
x	Coordinate along the sheet [m]
y	Coordinate normal to the sheet [m]

GREEK SYMBOLS

α	$\left(\frac{Q^*}{b\ \rho C_p}\right)$ heat source / sink parameter
α^*	Thermal diffusivity [m^2 s^{-1}]
η	Similarity variable
μ	Dynamic viscosity [kg $m^{-1}s^{-1}$]
υ	Kinematic fluid viscosity [m^2 s^{-1}]
ρ	Density [kg m^{-3}]
ψ	Stream function [m^2 s^{-1}]
σ	Electrical conductivity [mho m^{-1}]
$\sigma *$	Stefan-Boltzmann constant
ξ	Change of variable
τ_w	Wall shearing stress [m^2 s^{-1}]
θ	$\left(\frac{T-T_\infty}{T_w-T_\infty}\right)$ non-dimensional temperature (for the PST case)

REFERENCES

Abel MS, Siddheshwar PG, Nandeppanavar MM (2007). Heat transfer in a viscoelastic boundary layer flow over a stretching sheet with viscous dissipation and non-uniform heat source, International Journal of Heat and Mass Transfer 50, pp. 960–966.

Abel MS, Nandeppanavar MM (2007). Effects of radiation and non-uniform heat source on MHD flow of viscoelastic fluid and heat transfer over a stretching sheet, International Journal of Applied Mechanics and Engineering 12(4), pp. 903–918.

Abel MS, Nandeppanavar MM (2008a), Heat transfer in MHD viscoelastic boundary layer flow over a stretching sheet with space and temperature dependent heat source, International Journal of Applied Mechanics and Engineering 13(2), pp. 293–309.

Abel MS, Sanjayanand E, Nandeppanavar MM (2008b), Viscoelastic MHD flow and heat transfer over a stretching sheet with viscous and Ohmic dissipations. Communications in Nonlinear Science Numerical Simulation 13(9), pp. 1808–1821.

Abel MS, Nandeppanavar MM (2008c). Heat transfer in MHD viscoelastic fluid over a stretching sheet with variable thermal conductivity, non-uniform heat source and radiation, Applied Mathematical Modelling 32(10), pp. 1965–1983.

Abel MS, Nandeppanavar MM (2009). Heat transfer in MHD viscoelastic boundary layer flow over a stretching sheet with non-uniform heat source/sink, Communications in Nonlinear Science Numerical Simulation 14 (2009), pp. 2120–2131.

Akyildiz FT, Vajravelu K, Liao SJ (2009). A new method for homoclinic solutions of ordinary differential equations, Chaos, Solitons Fractals 39, pp. 1073–1082

Alderson JV, Caress JB, Sager RL (1968). The cooling rate of a glass fibre in the continuous filament process, Laboratory report No. 235 of Pilkington Brothers Limited, Lathom, Ormskirk, Lancashire, UK.

Ali ME (1995). On thermal boundary layer on a power law stretched surface with suction or injection, International Journal of Heat and Fluid Flow 16, pp. 280–290.

Alizadeh-Pahlavan A, Borjian-Boroujeni S (2008). On the analytical solution of viscous fluid flow past a flat plate, Physics Letters A 372, pp. 3678–3682.

Anderson L (1958). Cooling time of strong glass fibers, Journal of Applied Physics 29, pp. 9–12.

Arridge RGC, Prior K (1964). Cooling time of silica fibres, Nature, 203, pp. 386–387.

Banks WHH (1983). Similarity solutions of the boundary-layer equations for a stretching wall, ZAMM- Journal of Applied Mathematics and Mechanics 2, pp. 375–392.

Bég O Anwar, Bég TA, Takhar HS and Raptis A (2004). Mathematical and numerical modeling of non-Newtonian thermo-hydrodynamic flow in non-Darcy porous media, International Journal of Fluid Mechanics Research, 31, pp. 1-12.

Bég O Anwar, Takhar HS, Bharagava R, Rawat S and Prasad VR (2008a). Numerical study of heat transfer of a third grade viscoelastic fluid in non-Darcian porous media with thermophysical effects, Physica Scripta, 77, pp. 1-11.

Bég O Anwar, Takhar HS, Zueco J, Sajid A and Bhargava R (2008b). Transient Couette flow in a rotating non-Darcian porous medium parallel plate configuration: network simulation method solutions, Acta Mechanica, 200, pp. 129-144.

Bég O Anwar, Zueco J, Takhar HS, Bég TA and Sajid A (2009a). Transient non-linear optically-thick radiative-convective double-diffusive boundary layers in a Darcian porous medium adjacent to an impulsively started surface: network simulation solutions, Communications in Nonlinear Science and Numerical Simulation, 14, pp. 3856-3866.

Bég O Anwar, Zueco J, Bég TA, Takhar HS and Kahya E (2009b). NSM analysis of time-dependent nonlinear buoyancy-driven double-diffusive radiative convection flow in non-Darcy geological porous media, Acta Mechanica, 202, pp. 181-204.

Bég O Anwar, Sim L, Zueco J and Bhargava R (2010). Numerical study of magnetohydrodynamic viscous plasma flow in rotating porous media with Hall currents and inclined magnetic field influence, Communications in Nonlinear Science and Numerical Simulation, 15, pp. 345-359.

Bég O Anwar and Makinde OD (2011a). Viscoelastic flow and species transfer in a Darcian high-permeability channel, Petroleum Science and Engineering, 76, pp. 93–99.

Bég O Anwar, Prasad VR, Vasu B, Reddy NB, Li Q and Bhargava R (2011b). Free convection heat and mass transfer from an isothermal sphere to a micropolar regime with Soret/Dufour effects, Int. J Heat and Mass Transfer, 54, pp. 9-18.

Bég O Anwar, Zueco J and Chang TB (2011c). Numerical analysis of hydromagnetic gravity-driven thin film micropolar flow along an inclined plane, Chemical Engineering Communications, 198, pp. 312- 331.

Bég O Anwar, Bhargava R and Rashidi MM (2011d). Numerical Simulation in Micropolar Fluid Dynamics, Lambert Academic Publishing, Germany.

Bég O Anwar, Zueco J and Ghosh SK (2011e). Unsteady hydromagnetic natural convection of a short-memory viscoelastic fluid in a non-Darcian regime: network simulation. Chemical Engineering Communications, 198, pp. 172-190.

Bég O Anwar, Ghosh SK and Narahari M (2011f). Mathematical modelling of oscillatory MHD Couette flow in a rotating highly permeable medium permeated by an oblique magnetic field, Chemical Engineering Communications, 198, pp. 235-254.

Bég O Anwar, Bég Tasveer A, Rashidi MM and Asadi M (2012). Homotopy semi-numerical modelling of nanofluid convection flow from an isothermal spherical body in a permeable regime, International Journal of Microscale and Nanoscale Thermofluid Transport Phenomena, 3, pp. 237–66.

Bég Anwar O, Rashidi MM, Kavyani N and Islam MN (2013). Entropy generation in hydromagnetic convective Von Karman swirling flow: homotopy analysis, International Journal of Applied Mathematics and Mechanics, 9(4), pp. 37-65.

Bourne DE, Elliston DG (1970). Heat transfer through the axially symmetric boundary layer on a moving circular fibre, International Journal of Heat and Mass Transfer, 13, pp. 583–593.
Bourne DE, Dixon H (1971). The cooling of fibres in the formation process, International Journal of Heat and Mass Transfer 24, pp. 1323–1331.

Chen CK, Char MI (1988). Heat transfer of a continuous stretching surface with suction and blowing, Journal of Mathematical Analysis and Applications 135, pp. 568–580.

Chida K, Katto Y (1976). Study on conjugate heat transfer by vectorial dimensional analysis, International Journal of Heat and Mass Transfer 19(5), pp. 453–460.

Chowdhury MSH, Hashim I, Abdulaziz O (2009). Comparison of homotopy analysis method and homotopy-perturbation method for purely nonlinear fin-type problems. Communications in Nonlinear Science Numerical Simulation 14, pp. 371–378.

Cortell R (2007). MHD flow and mass transfer of an electrically conducting fluid of second grade in a porous medium over a stretching sheet with chemically reactive species. Chemical Engineering Proceedings, 46, pp. 721-725.

Crane LJ (1970). Flow past a stretching plate, ZAMP-Journal of Applied Mathematics and Physics 21, pp. 645–647.

Das D, Sen K, Saraogi A, Maity S (2010). Experimental studies on electro-conductive fabric prepared by in situ polymerization of thiophene onto polyester, Journal of Applied Polymer Science, 116, pp. 3555–3561.

Dinarvand S, Rashidi MM (2010). A reliable treatment of a homotopy analysis method for two-dimensional viscous flow in a rectangular domain bounded by two moving porous walls, Nonlinear Analysis: Real World Applications 11, pp. 1502–1512.

Domairry G, Nadim N (2008). Assessment of homotopy analysis method and homotopy perturbation method in non-linear heat transfer equation. International Communications in Heat and Mass Transfer 35, pp. 93–102.

Domairry G, Mohsenzadeh A, Famouri M (2009). The application of homotopy analysis method to solve nonlinear differential equation governing Jeffery–Hamel flow, Communications in Nonlinear Science Numerical Simulation 14, pp. 85–95.

Domairry G, Fazeli M (2009). Homotopy analysis method to determine the fin efficiency of convective straight fins with temperature-dependent thermal conductivity, Communications in Nonlinear Science Numerical Simulation 14(2), pp. 489–499.

Dutta BK, Roy P, Gupta AS (1985). Temperature field in flow over a stretching sheet with uniform heat flux, International Communications in Heat and Mass Transfer 12, pp. 89–94.

Erickson LE, Fan LT, Fox VG (1966). Heat and mass transfer on a moving continuous flat plate with suction or injection, Industrial and Engineering Chemical Fundamentals 5, pp. 19–25.

Glicksman LR (1968). The cooling of glass fibres, Glass Technology 9, pp. 131–138.

Griffin JF, Throne JL (1967). On thermal boundary layer growth on continuous moving belts, Journal of Artificial Intelligence in Chemical Engineering 13, pp. 1210–1211.

Griffith RM (1964). Velocity, temperature and concentration distributions during fiber spinning, Industrial and Engineering Chemical Fundamentals 3, pp. 245–250.

Gupta PS, Gupta AS (1977). Heat and mass transfer on a stretching sheet with suction or blowing, Canadian Journal of Chemical Engineering 55, pp. 744–746.

He, JH (2000) A coupling method for homotopy technique and perturbation technique for non-linear problem, International Journal of Non-Linear Mechanics 35, pp. 37-43.

He JH (2006). Homotopy perturbation method for solving boundary value problems, Physics Letters A 350, pp. 87-88.

Horvay G (1961). Temperature distribution in a slab moving from a chamber at one temperature to a chamber at another temperature, ASME Journal of Heat Transfer 83, pp. 391–402.

Horvay G, Dacosta I (1964). Temperature distribution in a cylindrical rod moving from a chamber at one temperature to a chamber at another temperature, ASME Journal of Heat Transfer 86, pp. 265–270.

M. Husain, T. Hayat, C. Fetecau, S. Asghar, On accelerated flows of an Oldroyd-B fluid in a porous medium, Nonlinear Analysis Real World Applications 9 (2008) 1394–1408.

Son KJ and Fahrenthold EP (2012). Evaluation of magnetorheological fluid augmented fabric as a fragment barrier material, Smart Materials and Structures, 21, pp. 075012.

Liao SJ (1999). An explicit, totally analytic approximate solution for Blasius' viscous flow problems, International Journal of Non-Linear Mechanics 34, pp. 759–778.

Liao SJ (2003). Beyond Perturbation: Introduction to Homotopy Analysis Method, Boca Raton Chapman & Hall/CRC Press, Florida, USA.

Liao SJ (2005). A new branch of solutions of boundary-layer flows over a stretching flat plate, International Journal Heat and Mass Transfer 49, pp. 2529–2539.

Liao SJ (2009). Notes on the homotopy analysis method: some definitions and theorems, Communications in Nonlinear Science Numerical Simulation 14, pp. 983–997.

McLeod JB, Rajagopal KR (1987). On the uniqueness of flow of a Navier–Stokes fluid due to a stretching boundary, Archive for Rational Mechanics and Analysis 98, pp.385–393.

Mehmood A, Ali A, Takhar HS, Bég O Anwar, Islam MN and Wilson LS (2010). Unsteady von Karman swirling flow: semi-analytical study using the homotopy analysis method, International Journal of Applied Mathematics and Mechanics, 6, pp.67–84.

Chandraskehar, S (1960). Radiative Transfer, Clarendon, New York, USA.

Öziş T and Yıldırım A (2007). A comparative study of He's Homotopy perturbation method for determining frequency-amplitude relation of a non-linear oscillator with discontinuities, Communications in Nonlinear Science Numerical Simulation. 8 (2), pp. 243- 248.

Rashidi MM, Mohimanian Pour SA and Abbasbandy S (2011). Analytic approximate solutions for heat transfer of a micropolar fluid through a porous medium with radiation, Communications in Nonlinear Science Numerical Simulation 16, pp. 1874–1889.

Rashidi MM, Mohimanian Pour SA (2010). Analytic approximate solutions for unsteady boundary-layer flow and heat transfer due to a stretching sheet by homotopy analysis method, Nonlinear Analysis: Modelling and Control 15, pp. 83–95.

Rashidi MM, Domairry G, Dinaarvand S (2009). Approximate solutions for the Burger and regularized long wave equations by means of the homotopy analysis method, Communications in Nonlinear Science Numerical Simulation 14, pp. 708–717.

Rawat S, Bhargava R, Bhargava Renu and Bég O Anwar (2009). Transient magneto-micropolar free convection heat and mass transfer through a non-Darcy porous medium channel with variable thermal conductivity and heat source effects, Proc. IMechE Part C-Journal of Mechanical Engineering Science, 223, pp. 2341-2355.

Rice RG and Do DD (1994). Applied Mathematics for Chemical Engineers, Wiley Series in Chemical Engineering, New York, USA.

Rossow VJ (1958). On the flow of electrically conducting fluids over a flat plate in the presence of a transverse magnetic field, NASA Report-489-508.

Sakiadis BC (1961). Boundary-layer behavior on continuous solid surfaces, Journal of Artificial Intelligence in Chemical Engineering 7, pp. 26–28.

Sajid M, Hayat T (2008). Comparison of HAM and HPM methods in nonlinear heat conduction and convection equations, Nonlinear Analysis Real World Applications 9, pp. 2296–2301.

Takhar HS, Bég O Anwar, Chamkha AJ, Filip D and Pop I (2003). Mixed radiation-convection boundary layer flow of an optically-dense fluid along a vertical plate in a non-Darcy porous medium, International Journal of Applied Mechanics and Engineering, 8, pp. 483-496.

Tripathi D, Bég O Anwar and Curiel-Sosa JL (2012). Homotopy semi-numerical simulation of peristaltic flow of generalised Oldroyd-B fluids with slip effects, Computer Methods in Biomechanics and Biomedical Engineering.DOI:10.1080/ 10255842. 2012. 688109

Tsou FK, Sparrow EM, Goldstein RJ (1967). Flow and heat transfer in the boundary layer on a continuously moving surface, International Journal of Heat and Mass Transfer 10, pp. 219–234.

Vasudevan G, Middleman S (1970). Momentum, heat and mass transfer to a continuous cylindrical surface in axial motion, Journal of Artificial Intelligence in Chemical Engineering 16, pp. 614–619.

Viskanta R (1963). Interaction of heat transfer by conduction, convection and radiation in a radiating fluid, ASME Journal of Heat Transfer, 44, pp. 318-329.

Wang C, Zhu JM, Liao SJ and Pop I (2003a). On the explicit analytic solution of Cheng–Chang equation. International Journal of Heat and Mass Transfer 46, pp. 1855–1860.

Wang C, Liao SJ, Zhu J (2003b). An explicit solution for the combined heat and mass transfer by natural convection from a vertical wall in a non-Darcy porous medium, International Journal of Heat and Mass Transfer 46, pp. 4813–4822.

Wang J, Chen JK, Liao SJ (2008). An explicit solution of the large deformation of a cantilever beam under point load at the free tip, Journal of Computational Applied Mathematics 212, pp. 320–330.

Zueco J and Bég O Anwar (2011). Network numerical simulation of hydromagnetic Marangoni mixed convection boundary layers, Chemical Engineering Communications 198, pp. 552-571.